Secondary reactions of aromatics-derived oxygenated organic molecules lead to plentiful highly oxygenated organic molecules within an intraday OH exposure

Yuwei Wang[1], Yueyang Li[1], Gan Yang[1], Xueyan Yang[1], Yizhen Wu[1], Chuang Li[1], Lei Yao[1,2], Hefeng, Zhang[3*], Lin Wang[1,2,4,5,6] *

[1] Shanghai Key Laboratory of Atmospheric Particle Pollution and Prevention (LAP[3]), Department of Environmental Science and Engineering, Jiangwan Campus, Fudan University, Shanghai 200438, China

[2] Shanghai Institute of Pollution Control and Ecological Security, Shanghai 200092, China

[3] State Environmental Protection Key Laboratory of Vehicle Emission Control and Simulation, Vehicle Emission Control Center of Ministry of Ecology and Environment, Chinese Research Academy of Environmental Sciences, Beijing 100012, China

[4] IRDR International Center of Excellence on Risk Interconnectivity and Governance on Weather/Climate Extremes Impact and Public Health, Fudan University

[5] National Observations and Research Station for Wetland Ecosystems of the Yangtze Estuary, Shanghai, China

[6] Collaborative Innovation Center of Climate Change, Nanjing, 210023, China

Corresponding Author: H.Z., email, zhanghf@craes.org.cn; phone, +86-10-84915586
L.W., email, lin_wang@fudan.edu.cn; phone, +86-21-31243568

ABSTRACT. Highly oxygenated organic molecules (HOMs) can participate in new particle formation (NPF) and enhance growth of newly formed particles partially because of their low volatility. Previous studies have shown formation of HOMs via autoxidation reactions of RO_2 intermediates generated by OH-initiated oxidation of anthropogenic volatile organic compounds (VOCs). It was also suggested that multi-generation OH oxidation could be an important source for aromatics-derived HOMs. However, our understanding on the generation of aromatics-derived HOMs are still insufficient, especially for their formation mechanisms, which determine molar yields of HOMs and are essential to the establishment of global chemical box models related to HOMs. In this study, with a potential aerosol formation oxidation flow reactor (PAM OFR), a series of OH-initiated oxidation experiments of 1,3,5-trimethylbenzene (1,3,5-TMB) were conducted to investigate the influences of the extent of OH exposure on the formation of aromatics-derived HOMs. The evolution of oxidation products of 1,3,5-TMB in an OH exposure range of $(0.5 - 5.0) \times 10^{10}$ molecules cm^{-3} s, equivalent to an OH exposure of $0.7 - 6.9$ hours at an OH concentration of 2×10^6 molecules cm^{-3}, was investigated by a nitrate-based chemical ionization mass spectrometer and a Vocus proton-transfer-reaction mass spectrometer, indicating significant secondary OH chemistry

37 during the ageing of stabilized first generation oxygenated products within an intraday OH
38 exposure and formation of various HOMs with more oxygen content and thus lower volatility.
39 In addition, organonitrates, formed after the introduction of NO_x into the reaction systems,
40 further confirmed the existence of such secondary reactions. Our study suggests an important
41 role of secondary OH chemistry in the oxidation of aromatics and elucidates detailed formation
42 mechanisms of certain HOM products.

43

44 **1 Introduction**

45   OH radicals can react with volatile organic compounds (VOCs) in the atmosphere,
46 converting primary pollutants to secondary ones. Generated from oxidation of VOCs,
47 oxygenated organic molecules (OOMs) are crucial in a variety of atmospheric chemical
48 processes, contributing efficiently to the formation of secondary organic aerosols (SOAs) and
49 ground-level O_3 (Ng et al., 2010; Wang et al., 2022; Qu et al., 2021). Among the enormous
50 number of oxygenated VOCs (OVOCs), highly oxygenated organic molecules (HOMs) have
51 recently attracted significant attention (Bianchi et al., 2019). Most of HOMs are low volatile
52 organic compounds (LVOCs) or extremely low volatile organic compounds (ELVOCs), and
53 thus are able to drive the initial formation of nucleated particles under certain conditions and
54 contribute to the subsequent growth of newly-formed particles, which finally enhance SOA
55 formation (Tröstl et al., 2016; Lehtipalo et al., 2018; Stolzenburg et al., 2018; Mohr et al., 2019;
56 Qiao et al., 2021).

57   Formation of HOMs is typically triggered by oxidation of VOCs in the gas phase. Peroxy
58 radicals (RO_2) are generated at the initial step and will undergo an intramolecular hydrogen
59 atom shift forming a hydroperoxide functionality and an alkyl radical. A molecular oxygen will
60 rapidly attach to this alkyl radical and form a new and more oxidized RO_2. This reaction is
61 called as autoxidation and the newly formed RO_2 can go through another autoxidation or
62 bimolecular termination reactions to form a stabilized product (Crounse et al., 2013).
63 Autoxidation is suggested to be responsible for widely detected HOMs in the atmosphere,
64 because it can form highly oxygenated RO_2 in a short time scale. In terms of biomolecular
65 reactions, RO_2 reacts appreciable only with hydroperoxyl radical (HO_2), NO, and another RO_2.
66 The RO_2 reaction chain in polluted areas is largely terminated by NO, which prohibits
67 generation of compounds with high oxidation levels and reduces yields of HOMs (Bianchi et
68 al., 2019).

69   Nevertheless, autoxidation reactions alone are not enough to explain the large numbers of
70 oxygen atoms in HOMs observed in laboratory experiments and ambient campaigns. Take
71 alkylbenzenes as an example, previous studies suggest that the main products of OH-initiated

72 oxidation of alkylbenzenes (C_xH_{2x-6}, x=7, 8, or 9), i.e., bicyclic peroxy radicals (BPR, $C_xH_{2x-6}O_5\cdot$,

73 x=7, 8, or 9) (Jenkin et al., 2003), can undergo an autoxidation reaction and form a new

74 peroxy radical, $C_xH_{2x-6}O_7\cdot$ (x=7, 8, or 9) (Wang et al., 2017).The autoxidation of BPR could be

75 fast if it has a favorable structure, as found in a previous study (Wang et al., 2017). On the

76 other hand, the structure of resulting $C_xH_{2x-6}O_7\cdot$ is strongly different from that of BPR, whose

77 autoxidation reaction rate can be as low as the order of 0.001 s^{-1}, since it lacks enhancements

78 from favorable transition state geometries and substitutes or resonance structures (Bianchi et

79 al., 2019; Otkjær et al., 2018). Such a slow autoxidation reaction rate cannot explain the

80 extensive existence of HOM monomers with more than 7 oxygen atoms and HOM dimers with

81 more than 10 oxygen atoms, which are the maximum numbers of oxygen atoms in stabilized

82 monomer and dimer products, respectively, formed from $C_xH_{2x-6}O_7\cdot$ (Molteni et al., 2018;

83 Wang et al., 2020; Mentel et al., 2015). Another possibility is the formation of a second oxygen

84 bridge after the hydrogen shift of BPR (Molteni et al., 2018), but this reaction pathway would

85 not allow a further oxygenation reaction without a breakage of the carbon ring, which is also

86 unpromising. A very recent investigation offers new insights into the formation mechanism of

87 these products, indicating the molecular rearrangement of BPR can initiate a series of

88 autoxidation (Iyer et al., 2023). However, the formation mechanism of HOMs with a large

89 hydrogen atom number is still vague, e.g., monomer products with 16 hydrogen atoms in the

90 OH-initiated oxidation of TMB and with 14 hydrogen atoms in the OH-initiated oxidation of

91 xylene.

92 Multigeneration reactions of VOCs complicate HOMs' formation. Previous studies

93 indicate that HOMs can also be formed by sequential oxidation of stabilized first-generation

94 products of benzene and toluene (Garmash et al., 2020; Cheng et al., 2021). Garmash et al.

95 (2020) conducted OH oxidation experiments of benzene and toluene with an OH exposure

96 equivalent to atmospheric oxidation times of 10 hours – 15 days at OH concentrations of ~10^6

97 molecules cm^{-3}. Cheng et al. (2021) simulated oxidation of benzene and toluene with an OH

98 exposure equivalent to 2.4 – 19.4 days of atmospheric photochemical ageing. Certainly, such

99 extremely high OH exposures favor secondary OH chemistry and help to facilitate our

100 understanding on product distributions, but such a long timescale limits atmospheric

101 implications of their results, given the complex physical and chemical processes at night.

102 Compared to benzene and toluene, trimethylbenzene (TMB) is a precursor characterized

103 with much larger HOM molar yields when reacted with OH, and the abundance of TMB in the

104 atmosphere is unignorable (Molteni et al., 2018; Yuan et al., 2012). Previous laboratory

105 experiments on TMB-derived HOMs mainly focused on the autoxidation reactions of BPR and

106 the influences of NO$_x$, while the quantity of experiments was finite with a limited range of OH

107   exposure, bringing down the universality and applicability of conclusions (Tsiligiannis et al.,

108   2019; Wang et al., 2020). From the mechanism perspective, a number of HOM monomers with

109   more than 7 oxygen atoms detected in the OH-initiated oxidation of TMB were previously

110   assumed to be generated via multiple autoxidation reactions (Molteni et al., 2018). Nevertheless,

111   a subsequent OH oxidation of the first-generation oxygenated products might be more plausible

112   for the formation of HOM monomers with more than 7 oxygen atoms from the present point of

113   view. Indeed, laboratory experiments show that RO_2 formed during the second-generation OH

114   oxidation of the first-generation stabilized oxidation products can also undergo autoxidation

115   reactions, which entangles reaction mechanisms potentially involved in the formation of those

116   HOMs and justifies more investigations on the multigeneration OH oxidation of aromatics

117   (Wang et al., 2020). OH with an atmospheric concentration up to $6\times10^6 - 2.6\times10^7$ molecule

118   cm^{-3}, which is several times higher than the typical average atmospheric OH concentration,

119   1.5×10^6 molecule cm^{-3} (Jacob, 1999), has been frequently observed in both urban and suburban

120   environments in China (Tan et al., 2019; Lu et al., 2012)., leading to a realistic implication of

121   multigeneration OH oxidation. Therefore, it is imperative to study chemical characteristics of

122   formation reactions of HOMs at different OH exposures, especially those fewer than or

123   equivalent to one day of atmospheric oxidation.

124   In this study, a series of laboratory experiments were conducted on the OH-initiated

125   oxidation of 1,3,5-TMB, selected as an example of anthropogenic VOCs with an OH exposure

126   equivalent to atmospheric oxidation times of roughly 0.7 – 6.9 hours at an average daytime OH

127   radical concentration of 2.0×10^6 molecules cm^{-3}. A nitrate-based chemical ionization mass

128   spectrometer (nitrate CIMS) and a Vocus proton-transfer-reaction mass spectrometer (Vocus

129   PTR) were deployed to measure the oxidation products and the precursor, respectively. From

130   the evolution of oxygenated products, we explored secondary OH chemistry of stabilized first-

131   generation oxygenated products generated by the oxidation of 1,3,5-TMB. Furthermore, the

132   influence of NO on the formation of HOMs was investigated by introducing N_2O into the

133   reaction system via formation of organonitrates.

134   **2 Methods**

135   OH-initiated oxidation of 1,3,5-TMB was investigated in a potential aerosol formation

136   oxidation flow reactor (PAM OFR) system at $T = 298 \pm 1$ K and a pressure of 1 atm (Lambe et

137   al., 2015). The experimental settings in this study differed slightly from what were used

138   previously (Wang et al., 2020). Forty OH experiments (Exp. 1 – 40) and twenty-eight NO_x

139   experiments (Exp. 41 – 68) were performed, the experimental conditions of which are

140   summarized in Table S1, including concentrations of the precursor, ozone, and NO and NO_2.

141   The equivalent OH exposure in the OFR for each experiment was estimated according to the

precursor consumption, also listed in Table S1. OH exposures in the OFR were in the range of $(0.5 - 5.0) \times 10^{10}$ molecules cm^{-3} s, equivalent to atmospheric oxidation times of roughly $0.7 - 6.9$ hours for 1,3,5-TMB at an average daytime OH radical concentration of 2.0×10^6 molecules cm^{-3}. In contrast, the OH oxidation lifetime for 1,3,5-TMB is around 2.4 hours at the aforementioned atmospheric average daytime OH concentrations.

A home-made 1,3,5-TMB/N$_2$ cylinder was used as a stable gaseous precursor source in the experiments, from which the flow rate of 1,3,5-TMB/N$_2$ varied between $1 - 3$ sccm (standard cubic centimeter per minute, standard to 0 °C, 1 atm), leading to $28.9 - 62.7$ ppb of 1,3,5-TMB in the OH oxidation experiments (Table S1). A total flow of 15 slpm (standard liters per minute, standard to 0 °C, 1 atm) zero-gas generated by a zero-gas generator (model 737-13, Aadco Instruments Inc.), together with the 1,3,5-TMB/N$_2$ flow, was introduced into the OFR. The reaction time in this series of experiments was kept at around 53 s. The flow in the PAM OFR is laminar with a very low axial mixing, as characterized with a Taylor dispersion model in a previous study (Lambe et al., 2011). Among the 15 slpm zero-gas, 6 slpm was initially passed through a Nafion humidifier (Perma Pure Model FC100-80-6MSS) filled with ultra-pure water and finally converged with the main flow into the OFR to achieve and keep a desired RH of 20.0 ± 2.5 % in the OFR throughout all the experiments, and 2 slpm was initially passed through a separate ozone chamber, resulting in an initial ozone concentration of around $429 - 881$ ppb in the OFR. The OFR was operated with only the 254 nm lights on, under which the primary oxidant production reactions in the OFR were $O_3 + h\nu\ (254\ nm) \rightarrow O_2 + O(^1D)$ and $O(^1D) + H_2O \rightarrow 2OH$. After turning on of UV lights, a certain HOM compound is believed to be generated if its signal is more than 3 standard deviations of its background signal. If the fluctuations in the 1-min-averaged signals of both TMB in the Vocus PTR and typical HOMs (i.e., C$_9$H$_{14}$O$_7$(NO$_3$)$^-$) in the nitrate CIMS are within 2% during a 10-min period, we assume that a steady state has been reached. It usually took around no more than 2 minutes for the signals of HOMs to stabilize after the adjustment of UV lights. We typically monitored the reaction products for around 20 minutes for each experiment. An ozone monitor (Model 106-M, 2B technologies) and a trace-gas analyzer for NO-NO$_2$-NO$_x$ (Thermo, 42i-TL) were placed at the exit of the OFR to measure concentrations of ozone and NO$_x$, respectively.

Non-tropospheric VOC photolysis is a typical issue that should be taken into account when evaluating the settings of OFR laboratory experiments. Photolysis of the precursor and HOMs were evaluated, showing that photolysis was not a contributor to our observation. The photolysis rate of 1,3,5-TMB can be estimated based on the absorption cross-sections of 1,3,5-TMB at 254 nm (Keller-Rudek et al., 2013) and UV photon fluxes estimated by a chemistry model discussed in the following sections. The ratio of photolysis-to-OH reaction in our

177 experiments was merely 0.010 – 0.033. Hence, photolysis of 1,3,5-TMB was insignificant in

178 the OFR. For stabilized products such as HOMs, the cross sections of organic molecules are

179 usually ~ 3.9×10^{-18} - 3.9×10^{-17} cm^2 (Peng et al., 2016), while the reaction rate between OH and

180 the stabilized first-generation products are estimated to be around 1.28×10^{-10} molecule^{-1} cm^3 s^{-1}

181 ^{1}, as suggested by MCM (Jenkin et al., 2003). Hence, the ratio of photolysis rates of HOMs to

182 their secondary OH oxidation rates is estimated to be merely around 0.020 – 0.056.

183 For experiments with NO_x, 350 sccm N_2O (99.999%, Air Liquid) was added into the OFR

184 to produce and sustain NO_x mixing ratios at levels that were sufficiently high to be a competitive

185 sink for RO_2 radicals. NO and NO_2 were produced via the reaction $N_2O + O(^1D) \rightarrow 2NO$,

186 followed by the reaction $NO + O_3 \rightarrow NO_2 + O_2$. Two sets of irradiance intensities were chosen

187 for NO_x experiments, generally resulting in two NO_x levels, 1.8 ppb NO + 70 ppb NO_2 (Exp.

188 41 – 54) and 4.8 ppb NO + 120 ppb NO_2 (Exp. 55 – 68) at the exit of the OFR. With the aim to

189 slightly modify OH exposure but keep NO_x concentrations constant among each set of

190 experiments, the initial concentrations of 1,3,5-TMB were adjusted in a large range (16.7 – 84.1

191 ppb), as an increase in the precursor concentration corresponds to a larger sink for OH, while

192 RH and irradiances were not changed.

193 A nitrate CIMS (Ehn et al., 2014; Eisele and Tanner, 1993) and a Vocus PTR (Krechmer

194 et al., 2018) were deployed at the exit of the OFR to measure the oxidation products of 1,3,5-

195 TMB. These two mass spectrometers have been well characterized in a previous study (Wang

196 et al., 2020).

197 In this study, the sample flow rate for the nitrate CIMS was 8 slpm through a Teflon tube

198 with an outer diameter (OD) of 1/4 in. and a length of 70 cm. The sheath flow for the nitrate

199 CIMS was supplied by a zero-gas generator at a flow rate of 15 slpm. Mass resolution was

200 approximately 8000 for ions with m/z larger than 200 Th. HOMs generated from TMB

201 oxidation were charged in the ambient pressure interface region by collisions with nitrate

202 clusters, $(HNO_3)_x \cdot NO_3^-$ ($x = 0 – 2$), and detected by nitrate CIMS as clusters with NO_3^-, i.e.,

203 $HOM \cdot NO_3^-$ (Hyttinen et al., 2015). In addition, HOMs' signals were corrected with relative

204 transmission efficiencies of our nitrate CIMS obtained via a method reported previously

205 (Heinritzi et al., 2016). We followed the same sampling method of PAM OFR as those in

206 previous studies, in order to obtain a similar flow tube residence time distributions (RTDs) and

207 thus validate usage of a modified PAM_chem_v8 model to estimate concentrations of radicals

208 in the OFR as discussed below. We acknowledge that this is not a perfect sampling setting for

209 nitrate CIMS. However, the reduction in the sampling efficiencies of various HOMs is likely

210 to be close, if not identical, which keeps the distributions of HOMs.

Vocus PTR was applied to quantify precursor concentrations and measure volatile and intermediate volatility oxidation products. The focusing ion-molecule reactor (FIMR) was heated up and its temperature was maintained at 100 ℃ during the experiments. The FIMR can be operated under 2.0 mbar without a strong interference from corresponding water clusters when ionizing the neutral compounds. The Vocus front and back voltages were 650 V and 15 V, respectively, forming an axial voltage of 635V and a reduced electrical field (*E/N*, where E is the electric field strength and N is the number density of the buffer gas in FIMR) of 180 Td. The radio frequency (RF) voltages and frequency were set to be 450 V and 1.3 MHz, respectively. The sample flow was introduced to the Vocus PTR through a Teflon tube with an OD of 1/4 in. and a length of 120 cm from the OFR. A total sample flow of 1.4 slpm was maintained by a pump with an orifice to minimize the delay time of sampling, from which approximately 125 sccm was sampled into the FIMR through a capillary tube.

We did not quantify HOMs' concentrations. Since the inner diameters of PAM OFR, sampling tube, and the nitrate CIMS inlet were different, and two reducing unions were used during sampling, the estimation of the penetration efficiency and sampling efficiency of HOMs are of a significant uncertainty. The initial concentrations of TMB utilized in the experiments fluctuated slightly, which resulted from sample preparation processes, but generally were around 50 ppbv. We tried to minimize potential influences of the differences in the initial TMB concentrations on the signals of HOMs by normalizing the HOMs signals with the initial TMB signal. To precisely illustrate changes in the abundance of HOMs at different OH exposures, a normalized signal was chosen to present the abundance of detected HOMs, which is defined as the ratio of the signals of HOMs in the nitrate CIMS normalized by the reagent ions and the initial signal of 1,3,5-TMB, i.e., $S(HOMs)/S(TMB)$. $S(HOMs)$ is the signal of HOM detected by the nitrate CIMS normalized with the signal of reagent ions, whereas $S(TMB)$ is the initial signal of 1,3,5-TMB detected by the Vocus PTR.

To validate our settings, a PAM chemistry model (PAM_chem_v8), utilized widely in previous studies, were chosen with the latest updates to calculate radical profiles in our OFR (Li et al., 2015; Cheng et al., 2021; Wang et al., 2020; Mehra et al., 2020; Lambe et al., 2015, 2018; Peng and Jimenez, 2020; Lambe et al., 2017). This model is based on a photochemical box model that includes chemistry of photolysis of oxygen, water vapor, and other trace gases by the primary wavelengths of mercury lamps, and simplified VOC and RO_2 chemistry (Table S2), but further reactions of the first-generation stabilized products and the second-generation organic radicals are not considered. The detailed reactions involved with RO_2 include:

$$RO_2 + R'O_2 \rightarrow RO + R'O + O_2 \qquad (R1)$$

246	$RO_2 + R'O_2 \rightarrow R=O + R'OH + O_2$	$(R2)$
247	$RO_2 + R'O_2 \rightarrow ROH + R'=O + O_2$	$(R3)$
248	$RO_2 + R'O_2 \rightarrow ROOR' + O_2$	$(R4)$
249	$RO_2 + HO_2 \rightarrow ROOH + O_2$	$(R5)$
250	$RO_2 + OH \rightarrow Products$	$(R6)$
251	$RO_2 \xrightarrow{\text{isomerization}} Products$	$(R7)$
252	$RO_2 + NO \rightarrow RO + NO_2$	$(R8)$
253	$RO_2 + NO \rightarrow RONO_2$	$(R9)$
254	$RO_2 \rightarrow physical\ loss$	$(R10)$
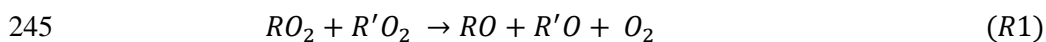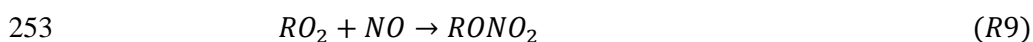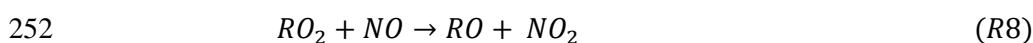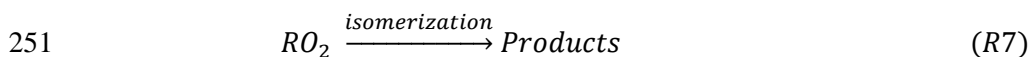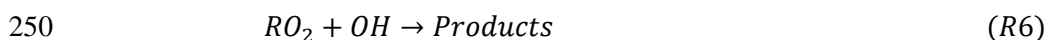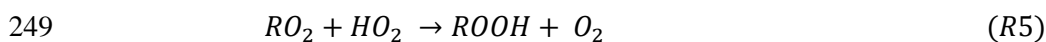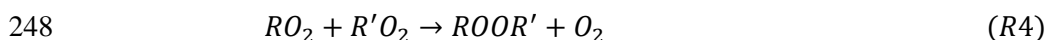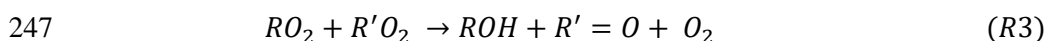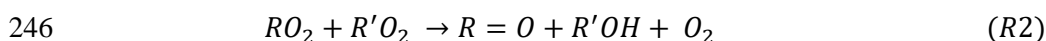
255      $R1$, $R2$, and $R3$ are reactions of $RO_2 + RO_2$, forming alkoxy radicals, carbonyl termination

256   products, and hydroxyl termination products, respectively. $R4$ is the accretion reaction,

257   forming dimers via combination of two monomeric RO_2. $R5$ is the reaction between RO_2 and

258   HO_2, forming hydroperoxyl radicals. $R6$ is the reaction between OH and RO_2, whose reaction

259   channels/products are proposed according to previous studies (Table S3). $R7$ is the

260   unimolecular reactions of RO_2 in the PAM OFR, among which the autoxidation reaction rate is

261   the most significant. $R8$ and $R9$ are the reactions between NO and RO_2, generating alkoxy

262   radicals and organonitrates, respectively. $R10$ is the physical loss of RO_2.

263   Kinetic data in the modified PAM_chem_v8 are obtained from the IUPAC (International

264   Union of Pure and Applied Chemistry) dataset (https://iupac-aeris.ipsl.fr, last access: 26

265   October 2023) and the MCM dataset (MCM v3.3.1, https://mcm.york.ac.uk/MCM/, last access:

266   9 October 2023), except those that are specifically discussed in details in the supplement. Note

267   that the total RO_2 concentration is simplified to be the sum of concentrations of BPR and

268      $C_9H_{13}O_7\cdot$. In this work, the autoxidation reaction and the accretion reaction of 1,3,5-TMB-

269   derived BPR, as well as the subsequent reactions of the autoxidation product of BPR, i.e.,

270      $C_9H_{13}O_7\cdot$, are newly implemented or modified in this model (Reaction No. 41 – 57 in Table

271   S2). The newly implemented or modified reactions in this model are discussed in

272   Supplementary Text S1. NO_x-related reactions are also included in the model. When we

273   simulate experiments without NOx, these reactions do not contribute to the simulation results.

274   The input parameters of temperature, mean residence time, water vapor concentration, O_3

275   concentration, and the initial 1,3,5-TMB concentration are 25 °C, 53 s, 0.8%, 500 ppbv, and 50

276   ppbv, respectively, as measured directly in the experiments. The actinic flux at 254 nm, I_{254}, is

277   constrained by comparing OH exposures by model output and OH exposures estimated by the

278   consumption of 1,3,5-TMB as measured by a Vocus PTR. Consumption of O_3 estimated by the

279   model agrees well with the measured results, with discrepancies being always within 10% at

280   different OH exposures.

281

3 Results and discussion

3.1 Validation of experiment settings

Concentration profiles of OH, RO_2, and HO_2 as a function of OH exposures in our experiments without NO_x are illustrated in Figure S1a. According to the modified PAM_chem_v8, when OH increased from 1.09×10^8 to 1.57×10^9 molecule cm^{-3}, HO_2 concentrations increased from 7.72×10^8 to 3.18×10^9 molecule cm^{-3}, whereas RO_2 concentrations increased from 4.83×10^9 to 8.48×10^9 molecule cm^{-3}. The radical concentrations in experiments with NO_x (Figure S1b) varied in a similar range, with RO_2 ranging from 3.89×10^9 to 9.34×10^9 molecule cm^{-3}, HO_2 ranging from 3.66×10^9 to 6.82×10^9 molecule cm^{-3}, and OH ranging from 4.83×10^8 to 9.05×10^8 molecule cm^{-3}, respectively. The ratios between HO_2/OH and RO_2/OH in our experiments are displayed in Figure S1c. The HO_2/OH ratio ranged between 1.9 and 7.1 in our PAM OFR experiments without NO_x, and the RO_2/OH ratio ranged between 4.9 and 47.9. In experiments with NO_x, the HO_2/OH ratio ranged between 3.7 and 17.9, whilst the RO_2/OH ratio ranged between 4.0 and 13.2. A recent comprehensive ambient campaign conducted in the wintertime central Beijing reported mean daytime peak concentrations of 8.8×10^7, 3.9×10^7, and 2.7×10^6 molecule cm^{-3} for total RO_2, HO_2, and OH, respectively (Slater et al., 2020), which corresponds to ambient RO_2/OH and HO_2/OH ratios of 32.6 and 14.4 (Figure S1c), respectively. Therefore, radical ratios in our flow tube were generally in the same order of magnitude with the ambient conditions.

301
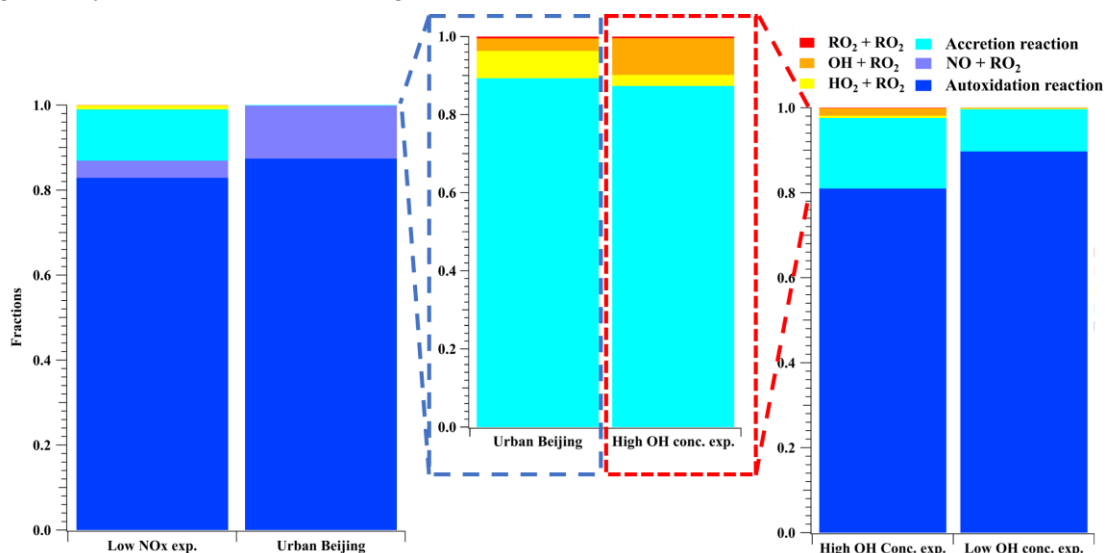
Figure 1. Fates of RO_2 generated in the low NO_x experiment (Exp. 44), urban Beijing (Slater et al., 2020), low OH and zero NO_x experiment (Exp. 19), and high OH and zero NO_x experiment (Exp. 12). Note that RO_2 fates of RO_2, OH, HO_2, and accretion channels are blown

305   up for a better comparison for urban Beijing and the high OH and zero NO_x experiment.

306   Reactions and kinetic rate coefficients used in the calculations are provided in Table S2.

307

308   We take Exp. 12, 19 and 44 as representative examples and compare simulation results

309 with those from the ambient environment (Slater et al., 2020). The RO_2 lifetime in urban Beijing

310 (Slater et al., 2020), low NO_x experiment, low OH and zero NO_x experiment, and high OH and

311 zero NO_x concentration experiment was 1.0, 0.7, 1.2, and 0.6 s, respectively. As shown in

312 Figure 1, In the low NO_x experiment (Exp. 44), the fractions of $RO_2 + RO_2$ ($R1 - R3$), accretion

313 reaction ($R4$), $RO_2 + HO_2$ ($R5$), $RO_2 + OH$ ($R6$), autoxidation ($R7$), and $RO_2 + NO$ ($R8 - R9$)

314 were 0.06%, 12.1%, 0.9%, 0.07%, 82.9%, and 4.0%, respectively. Calculated based on the

315 mean daytime peak concentrations of radicals in Beijing (Slater et al., 2020), the fractions of

316 $R1 - R3$, $R4$, $R5$, $R6$, $R7$, and $R8 - R9$ were 0.0005%, 0.09%, 0.007%, 0.003%, 87.4%, and

317 12.5%, respectively. For the experiment with low OH and zero NO_x (Exp. 19), the fractions of

318 $R1 - R3$, $R4$, $R5$, $R6$, and $R7$ were 0.05%, 10.0%, 0.15%, 0.14%, and 89.7%, respectively. For

319 the one with high OH and zero NO_x (Exp. 12), the fractions of $R1 - R3$, $R4$, $R5$, $R6$, and $R7$

320 were 0.08%, 16.6%, 0.54%, 1.8%, and 81.0%, respectively. The overall lifetimes of RO_2 and

321 the fractions of autoxidation together determine the significant and similar roles of

322 autoxidation in both laboratory experiments and the ambient. Therefore, the autoxidation chain

323 will run to a similar oxidation level between the laboratory and the ambient.

324   In experiments with NO_x (e.g., Exp. 44), though the yields of organonitrates were lower in

325 the laboratory experiments, the formation pathways of these compounds were the same as those

326 in the ambient. Based on the formulae of organonitrates, the detailed formulae for monomer

327 RO_2 could be probed, which helps to investigate the existence of multi-generation OH oxidation.

328 Alkoxy radicals generated in the NO termination channel will unlikely influence the

329 distributions of C9 stabilized products since they tend to get decomposed in the subsequent

330 reactions, as discussed in the Supplementary Text S1.

331   In experiments in absence of NO_x (e.g., Exp. 12 and 19), the proportions of $R8 - R9$, i.e.,

332 the NO channel in urban environment were reassigned to termination reactions of $R1 - R6$, i.e.,

333 $RO_2 + RO_2$, accretion reaction, $RO_2 + HO_2$, and $RO_2 + OH$. Comparison of relative fractions of

334 RO_2 fates of RO_2, OH, HO_2, and accretion channels (Figure 1) shows similarities between

335 laboratory and ambient results. By expanding proportions of these termination reactions,

336 laboratory investigations on distributions of products can be facilitated, as the detection of

337 certain HOM products became more precise and the mass spectra became simplified. As

338 discussed in the "results" session, products of $R2$, $R3$, and $R5$ channels of the main BPR were

339 not detected in our experiments due to their low oxygen contents, while secondary products

340 between products of $R2$, $R3$, and $R5$ channels of the main BPR and OH were observed.

341 Together with stabilized products and secondary products from $C_9H_{13}O_7\cdot$ (the peroxy radical

342 formed from autooxidation of BPR), secondary products between products of $R2$, $R3$, and $R5$

343 channels of the main BPR and OH help to elucidate the first- and multi-generation reaction

344 pathways in the 1,3,5-TMB+OH system, according to their molecular formular.

345   On the other hand, the much-expanded proportion of HOM dimers through accretion

346 reactions makes it inadequate to compare yields of HOM dimers and HOM monomers.

347 However, identification of HOM dimers can help us identify the exact RO_2 in the OFR and

348 confirm the conditions of secondary OH oxidation according to the number of hydrogen atoms

349 in the molecules.

350 3.2 Oxidation products

351   A total of 33 HOM monomers with formulae of $C_{7-9}H_{8-16}O_{6-11}$ and 22 HOM dimers with

352 formulae of $C_{17-18}H_{24-30}O_{8-14}$ were observed in the gas phase OH-initiated oxidation of 1,3,5-

353 TMB in the OFR, as listed in Table S4. The relative signal contributions of HOMs to the total

354 signals of all HOMs at an OH exposure of 2.38×10^{10} molecules cm^{-3} s are listed as an example

355 in Table S4. The most abundant HOM products were also shown in stack in Figure 2, whose

356 relationships with OH exposures are superimposed by a gamma function ($f(x) = ax^m e^{-x}$)

357 simulation line to guide the eyes. The sum of normalized HOM monomers' abundance

358 increased monotonically up to the highest OH exposure of 5×10^{10} molecule cm^{-3} s, whereas

359 those of HOM dimers showed a non-monotonic dependence on OH exposure. The observed

360 faster increase of accretion products than that of HOM monomers can be explained jointly by

361 the fast second-order kinetics for accretion reactions of RO_2 (Berndt et al., 2018b) and the high

362 concentrations of relevant radicals in this work. On the other hand, most of the first-generation

363 HOM dimers formed from accretion reactions contain at least one C=C bond and have more

364 functionalities than HOM monomers, and thus should be more reactive to OH radicals, which,

365 together with a faster deposition loss of dimers, results in a faster consumption of HOM dimers

366 than monomers in the OFR. The faster production and consumption of HOM dimers allowed

367 their concentrations to summit at middle levels of OH exposures. Because of the inherent

368 disadvantage of laboratory experiments, RO_2 concentrations are always too high in the OFR,

369 which has been pointed out in a previous study (Bianchi et al., 2019). The accretion reactions

370 in the OFR are relatively more significant than it should be in the ambient atmosphere. We do

371 not mean to compare HOM monomer and HOM dimer signals crossly here, but to pay attention

372 to their formulae.

373 (a)
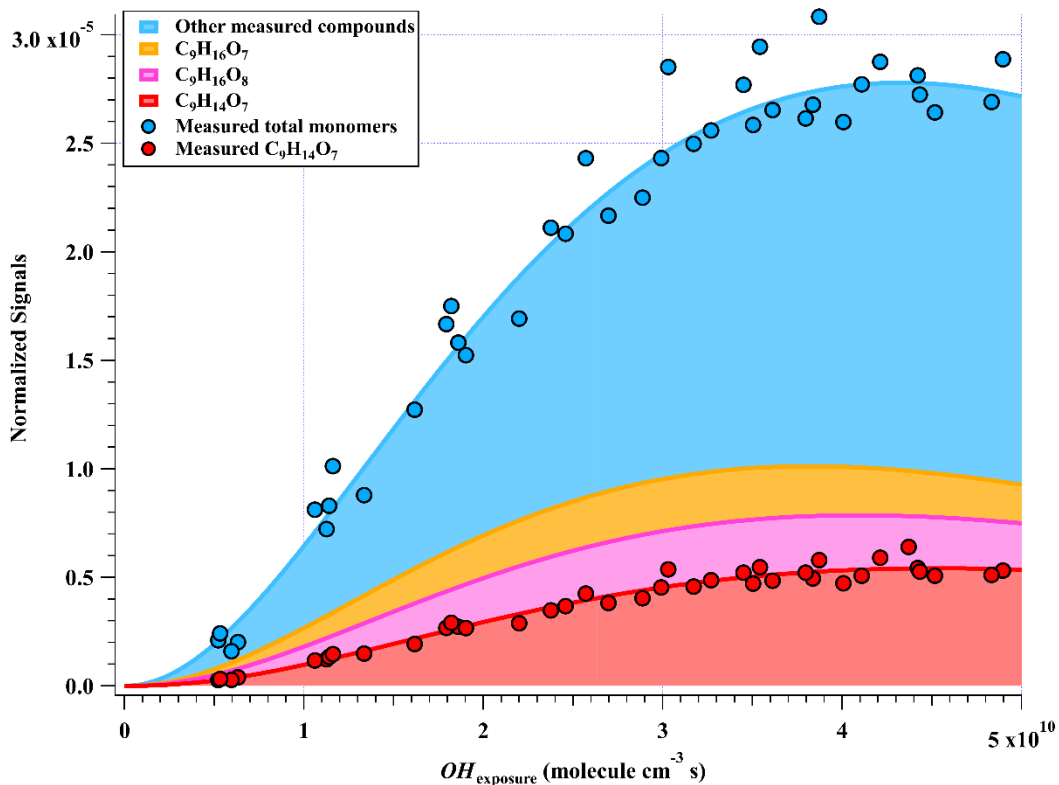
374

375   (b)
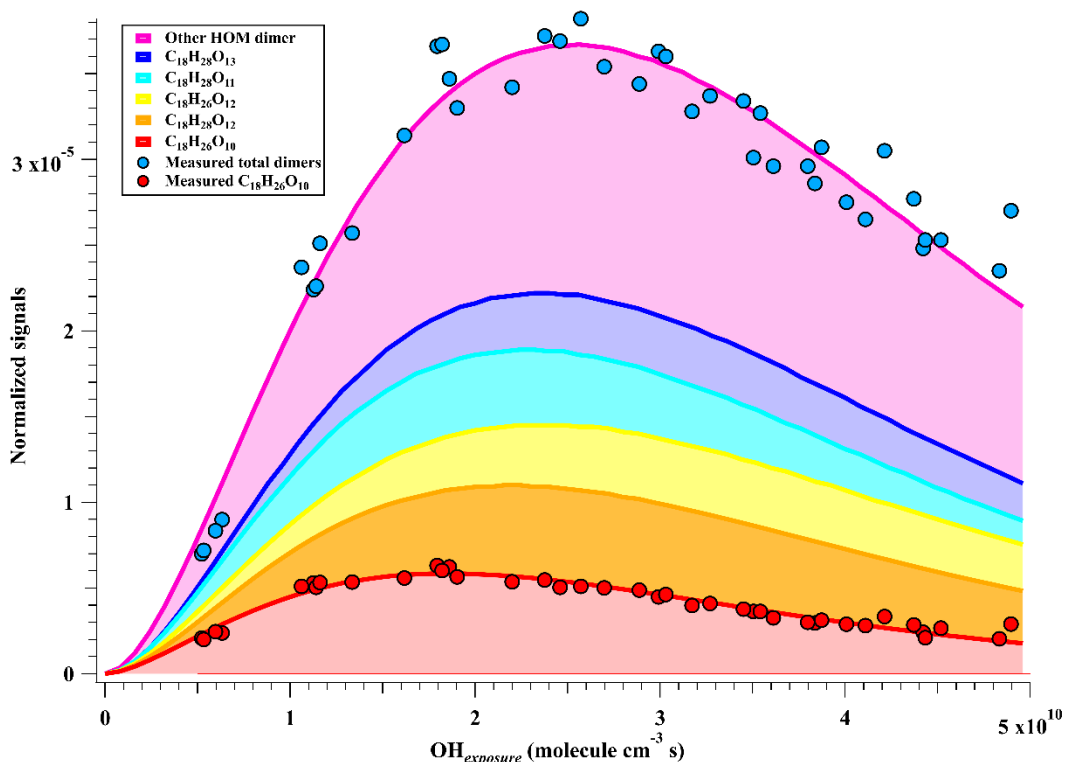
376

377   **Figure 2.** Normalized signals of (a) HOM monomers and (b) HOM dimers versus OH exposure

378   that are fitted via a gamma function and shown in stacked.

379

380 Theoretically, at a given RH and UV (i.e., a given OH), an increase in the initial TMB

381 would lead to formation of more RO_2, which corresponds to a larger RO_2/OH. However, under

382 our experimental conditions, the RO_2/OH/HO_2 channels of RO_2 radicals are always minor, and

383 thus an increase in RO_2/OH would not have a significant impact on the relative distribution of

384 products formed from these channels We compared product MS for experiments with a similar

385 OH exposure but different initial concentrations of TMB (e.g., Exp. 3 v.s. Exp. 19, and Exp. 12

386 v.s. Exp. 22). The OH exposures of Exp. 3 and Exp. 19 were estimated by the modified

387 PAM_chem_v8 model to be 5.2×10^9 and 5.3×10^9 molecule cm^{-3} s, respectively, but the initial

388 concentration of TMB of Exp. 3 was 25% more than that in Exp. 19. Meanwhile, the OH

389 exposures of Exp. 12 and Exp. 22 were 4.5×10^{10} and 4.4×10^{10} molecule cm^{-3} s, respectively,

390 but the initial concentration of TMB of Exp. 12 was 48% more than that in Exp. 22.

391 Comparisons between the product MS of Exp. 3 and Exp. 19 (Figure S2), as well as of Exp. 12

392 and Exp. 22, show that increase in the initial concentration of precursors generally resulted in

393 a minor increment in the absolute signals of HOMs. Clearly, the relative distributions of

394 products in these experiments are quite similar, indicating a minor difference in the relative

395 distributions of products caused by fluctuations of initial concentrations of TMB.

396 3.2.1 HOM monomers

397 Previous studies indicate that oxidation products derived from the peroxide-bicyclic

398 pathway represent a main fraction of HOMs (Wang et al., 2017; Zaytsev et al., 2019). For 1,3,5-

399 TMB, this pathway, as recommended by Master Chemical Mechanism (MCM), starts from a

400 BPR, $C_9H_{13}O_5\cdot$ (MCM name: TM135BPRO2) (Molteni et al., 2018). Scheme 1 has been

401 proposed to provide a good understanding of this reaction system and the structures of oxidation

402 products. Molteni et al. (2018) suggested that $C_9H_{13}O_7\cdot$, i.e., peroxy radical formed from

403 autooxidation of $C_9H_{13}O_5\cdot$ has two isomers. A second-step of endo-cyclization is required in

404 the formation of one of the isomer, which is extremely slow and not competitive as shown in

405 several previous studies using both experimental and theoretical approaches (Wang et al., 2017;

406 Xu et al., 2020). Even if such a second O_2 bridging to a double bond is assumed to be possible,

407 the abundance of this isomer should be significantly smaller than the other one, because of the

408 much faster reaction rate of H-shift reaction. Therefore, we do not take the $C_9H_{13}O_7\cdot$ isomer

409 containing a double endo-cyclization into consideration in this work. The majority of HOM

410 monomers is generated from subsequent reactions of $C_9H_{13}O_5\cdot$ and newly formed $C_9H_{13}O_7\cdot$,

411 both of which contain one C=C bond in the carbon backbone and thus have a feasible site for

412 OH addition. Meanwhile, the autoxidation reaction rate for newly formed $C_9H_{13}O_7\cdot$ should be

413 significantly smaller than $C_9H_{13}O_5\cdot$, as there is no hydrogen atom in $C_9H_{13}O_7\cdot$ that is able to

414 undergo a hydrogen atom shift at an appreciable rate based on our current understanding.

415 Therefore, the subsequent autoxidation reaction should not be able to generate large amounts
416 of more oxidized RO_2.

417

Scheme 1. Oxidation pathways of the bicyclic peroxy radical $C_9H_{13}O_5\cdot$ (MCM name:
TM135BPRO2) in the OH-initiated oxidation of 1,3,5-TMB. Green, blue, and black formulae
denote alkyl peroxy radicals, alkoxy radicals and stabilized products, respectively. Black
arrows denote the autoxidation pathway. MCM names for HO_2- and RO_2-termination products
of TM135BPRO2 are present.

423

424 The monomeric termination products of BPR, as shown in Scheme 1, were not detected
425 by nitrate CIMS due to their own low oxygen content and thus relative low detection efficiency
426 in nitrate CIMS, which has been investigated in a previous study (Riva et al., 2019). Those of
427 $C_9H_{13}O_7\cdot$ were all observed clearly, including $C_9H_{12}O_6$, $C_9H_{14}O_6$, and $C_9H_{14}O_7$. Especially,
428 $C_9H_{14}O_7$ was the most abundant one among all of the HOM monomer products (Figure 2a). As
429 proved by a previous study, these three species should be typical first-generation stabilized

430 products derived from autoxidation (Wang et al., 2020). These HOM monomers should consist

431 of several isomers bearing the same formula, because products from the secondary reactions

432 cannot share the same structure as that of the one from the first-generation reaction. However,

433 limited by the inherent disadvantages of mass spectrometers, we could not distinguish isomers

434 here and further illustrate their different chemical behaviors.

435   In addition to these three ones, the next most prominent products to $C_9H_{14}O_7$ were $C_9H_{16}O_7$

436 and $C_9H_{16}O_8$ (Figure 3a), which are produced from multi-generation oxidation according to

437 their hydrogen content (Molteni et al., 2018; Cheng et al., 2021). Based on the formulae of

438 these three HOM monomers, they ($C_9H_{14}O_7$, $C_9H_{16}O_7$, and $C_9H_{16}O_8$) could be formed from the

439 bimolecular termination reactions of $C_9H_{15}O_8^\bullet$, which can be generated by an OH attack to

440 $C_9H_{14}O_5$ (Scheme 2), the hydroperoxyl termination product of the BPR $C_9H_{13}O_5^\bullet$. The other

441 HOM monomers characterized with high signals were $C_9H_{14}O_8$ and $C_9H_{16}O_9$ (Figure 3b). These

442 two HOM monomers ($C_9H_{14}O_8$ and $C_9H_{16}O_9$), together with $C_9H_{16}O_8$, correspond to the

443 monomeric termination products of $C_9H_{15}O_9^\bullet$, which is highly likely the peroxy radical

444 generated by an OH attack to $C_9H_{14}O_6$ (Scheme 3), i.e., the hydroxyl termination product of

445 $C_9H_{13}O_7^\bullet$. As discussed earlier, $C_9H_{13}O_7^\bullet$ is a typical autoxidation reaction product of the BPR

446 of $C_9H_{13}O_5^\bullet$. Therefore, detected signals of $C_9H_{16}O_8$ should be the sum of two isomers' signals

447 at least. Other HOM monomers were generally observed at much lower signals and thus were

448 not plotted individually.

449 (a)

450

451 (b)

452
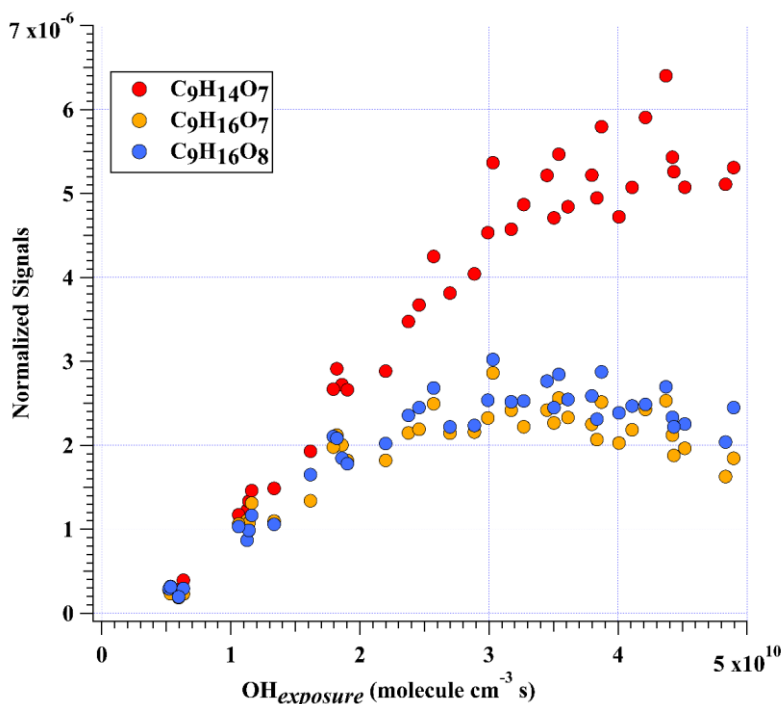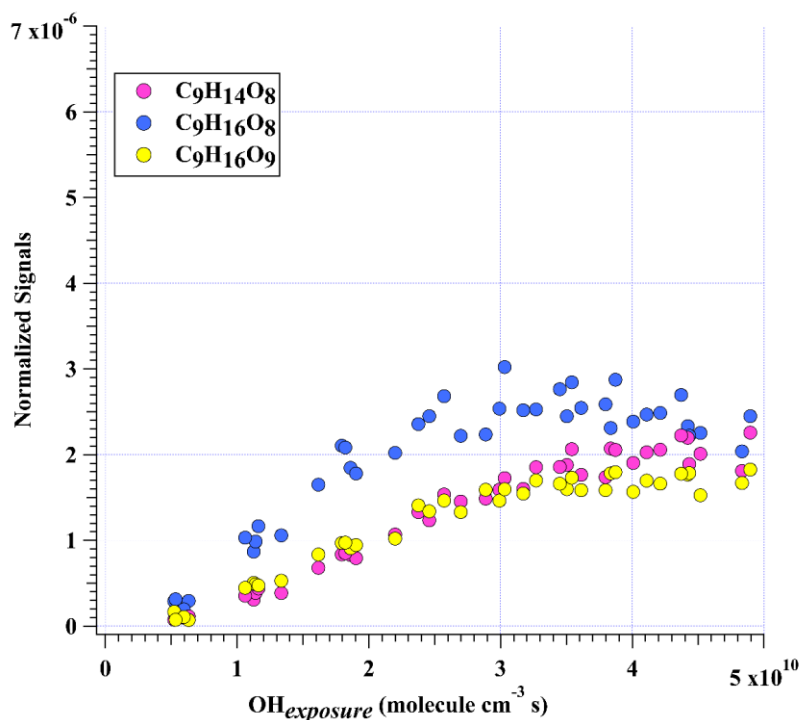
Figure 3. Normalized signals of (a) $C_9H_{14}O_7$, $C_9H_{16}O_7$, and $C_9H_{16}O_8$ and (b) $C_9H_{14}O_8$, $C_9H_{16}O_8$, and $C_9H_{16}O_9$ measured at the exit of OFR in experiments without NO_x as a function of OH exposure. $C_9H_{16}O_8$ are shown in both plots to better illustrate the chemical profiles of different compound groups.

457
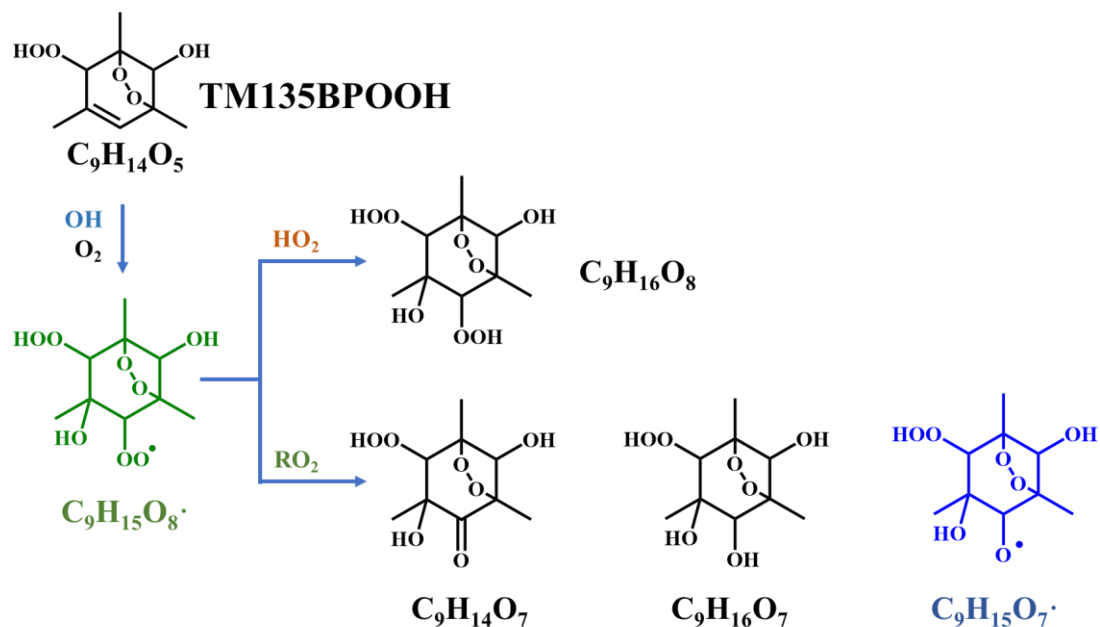
Scheme 2. Proposed formation pathways of $C_9H_{14}O_7$, $C_9H_{16}O_7$, and $C_9H_{16}O_8$ via the secondary OH oxidation of TM135BPOOH.
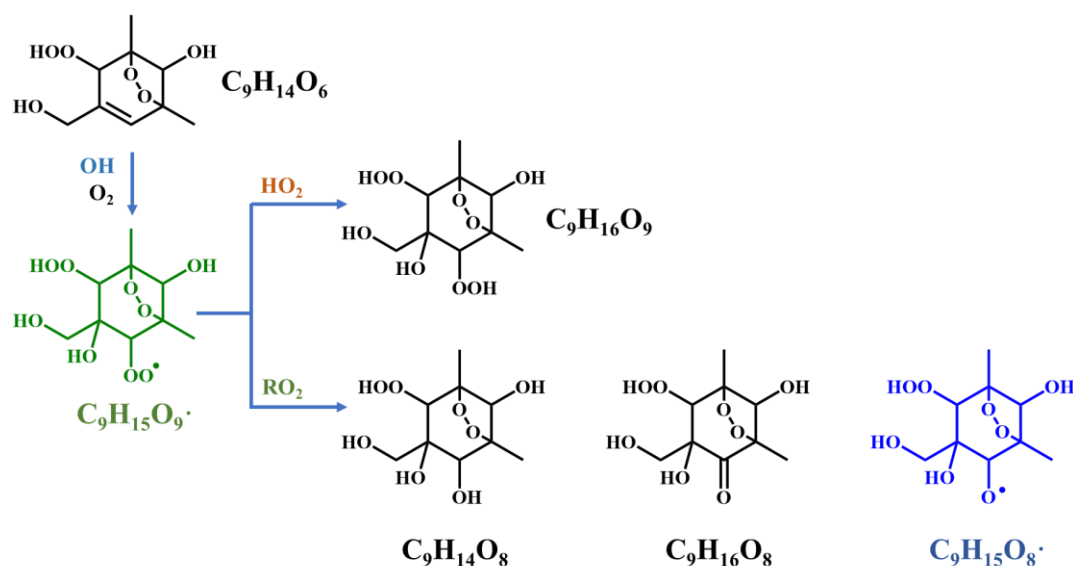
Scheme 3. Proposed formation pathways of $C_9H_{14}O_8$, $C_9H_{16}O_8$, and $C_9H_{16}O_9$ via the secondary OH oxidation of TM135BPOOH.

It is worth noting that HOM monomers with 18 hydrogen atoms were never observed in our experiments, including a potential stabilized hydroperoxyl products formed from $C_9H_{17}O_m\cdot$. This is expected, since $C_9H_{17}O_m\cdot$ should be in really low concentrations, if ever existed. As indicated by its hydrogen number, a $C_9H_{17}O_m\cdot$ was formed by at least two OH additions to the C=C bond of a $C_9H_{13}O_m\cdot$, but the main BPR, $C_9H_{13}O_5\cdot$, and its autoxidation product ($C_9H_{13}O_7\cdot$), are characterized with one C=C bond on the ring, which makes this formation pathway impossible. Other ring-breakage pathways should not contribute to the formation of this radical ($C_9H_{17}O_m\cdot$) because of their low branching ratio as determined by recent studies (Zaytsev et al., 2019; Xu et al., 2020).

Scheme 4 shows the NO termination pathways of the main BPR $C_9H_{13}O_5\cdot$ and its autoxidation product, $C_9H_{13}O_7\cdot$. After introducing N_2O into PAM OFR, quantities of organonitrates were generated, including both C9 and C18 organonitrates. The averaged mass spectrometry of nitrate CIMS in the 1.8 ppb NO experiment and 4.8 ppb NO experiment is shown in Figure S3. Organonitrates were formed via the NO + RO_2 reaction, called as NO termination reactions. The distribution of oxidation products under these two NO settings were similar.
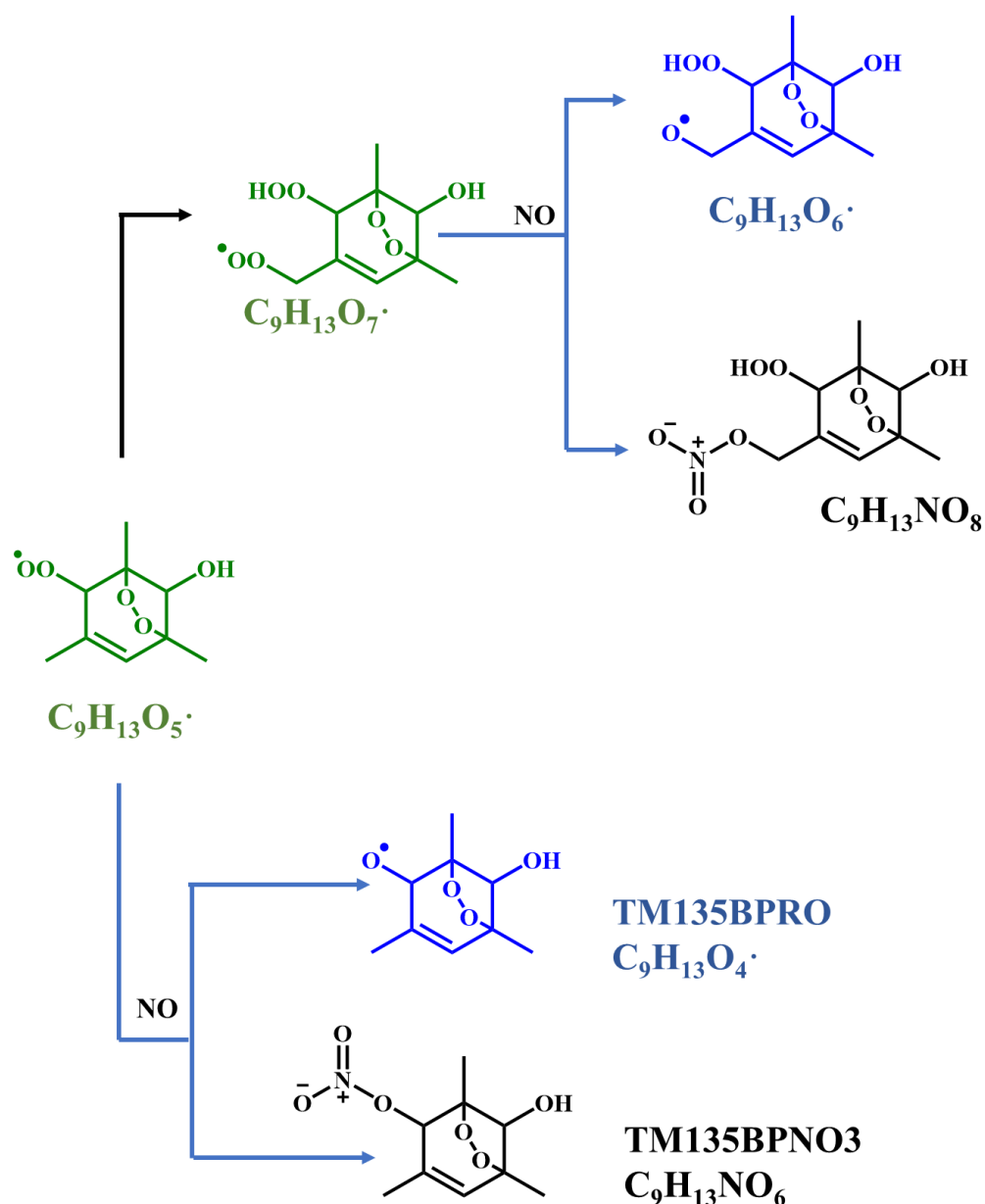
Scheme 4. NO termination reactions of the bicyclic peroxy radical $C_9H_{13}O_5\cdot$ (MCM name: TM135BPRO2) and its autoxidation reaction products. Green, blue, and black formulae denote alkyl peroxy radicals, alkoxy radicals and stabilized products, respectively. Black arrows denote the autoxidation pathway. MCM names of NO-termination products of TM135BPRO2 are present.

As discussed above, most of the first-generation HOMs should contain a C=C bond in the carbon backbone. The ubiquitous existence of organonitrates that contain two nitrogen atoms exactly confirms the extensive secondary OH oxidation in the systems, because the NO termination reaction of RO_2 is the only pathway that can generate organonitrates in our experiments and this pathway can only introduce one nitrogen atom at a time, as indicated in

Scheme 4. RO_2 can react with NO_2 to form peroxynitrates ($ROONO_2$) but these species are thermally unstable except at very low temperatures or when the RO_2 is an acylperoxy radical (Orlando and Tyndall, 2012), neither of which were not met in our experiments. The concentrations of NO_3 were estimated to be lower than 1 pptv by our modified PAM_chem_v8 because of the existence of decent concentrations of NO, which would consume NO_3 at a rapid reaction rate, i.e., 2.7×10^{-11} molecule^{-1} cm^3 s^{-1} (IUPAC dataset , https://iupac-aeris.ipsl.fr, last access: 26 October 2023). Therefore, NO_2 and NO_3 were not likely to react with RO_2 to form large amounts of organonitrates in our experiments. Taking the most abundant organonitrate, $C_9H_{14}N_2O_{10}$, as an example, it was exactly the NO termination product of $C_9H_{14}NO_9 \cdot$, which was generated from an OH attack and a subsequent O_2 addition to $C_9H_{13}NO_6$, the NO termination product of $C_9H_{13}O_5 \cdot$. For other organonitrates, $C_9H_{13}NO_8$, the second most abundant organonitrate, could be either a NO termination product of $C_9H_{13}O_7 \cdot$ or, together with other most abundant organonitrates, $C_9H_{15}NO_7$ and $C_9H_{15}NO_8$, classical termination products of $C_9H_{14}NO_9 \cdot$.

The $NO:RO_2$ ratio in the PAM OFR is lower than typical values in the ambient atmosphere, which is due to the existence of O_3 that was utilized to generate $O(^1D)$ in the OFR and its rapid reaction rate with NO. However, due to rapid reaction rate constants between NO and RO_2, i.e., around 8.5×10^{-12} molecule^{-1} cm^3 s^{-1}, the reaction rate for the NO termination channel of RO_2 was as fast as around $0.3 - 1.0$ s^{-1}. Large amounts of organonitrates would still be formed. Our conclusion is also valid because of detection of compounds with multiple nitrogen atoms.3.2.2 HOM dimers

Accretion reaction $RO_2 + RO'_2 \rightarrow ROOR' + O_2$ is a source of gas-phase dimer compounds from highly oxidized, functional RO_2 radicals.(Ehn et al., 2014; Berndt et al., 2018b; Zhao et al., 2018; Berndt et al., 2018a) $C_{18}H_{26}O_8$ and $C_{18}H_{26}O_{10}$ are two typical accretion reaction products in the 1,3,5-TMB + OH system, whose formation pathways have been elucidated.(Berndt et al., 2018b) $C_{18}H_{26}O_8$ can only be formed via the accretion reaction of two $C_9H_{13}O_5 \cdot$. $C_9H_{13}O_3 \cdot$ is not likely to react with $C_9H_{13}O_7 \cdot$ to form large amounts of $C_{18}H_{26}O_8$. $C_9H_{13}O_3 \cdot$ can only be formed after addition of a hydroxyl radical to the aromatic ring of 1,3,5-TMB and a subsequent O_2 addition to the newly formed hydroxyl-substituted cyclohexadienyl radical (Vereecken, 2019). However, the lifetime of this radical is extremely short, as $C_9H_{13}O_3 \cdot$ will undertake a ring-closure reaction and get attached by a O_2 very rapidly, forming BPR, $C_9H_{13}O_5 \cdot$. Its short lifetime and low concentration, as indicated by Berndt et al. (2018), lead to its insignificant role in the accretion reactions. In contrast, $C_{18}H_{26}O_{10}$ can be formed either by the accretion reaction between $C_9H_{13}O_5 \cdot$ and $C_9H_{13}O_7 \cdot$ or via a second OH attack to $C_{18}H_{26}O_8$. These two HOM dimers are so far the only ones that are confirmed to be formed via the

526 accretion reactions (Berndt et al., 2018b; Bianchi et al., 2019). There are currently no evidences

527 supporting that $C_9H_{15}O_m\cdot$ radicals can participate in the formation of HOM dimers with 28

528 hydrogens. Therefore, it hints that one could attribute the formation of $C_{18}H_{28}O_m$ to multi-

529 generation OH oxidation of $C_{18}H_{26}O_m$.

530      $C_{18}H_{26}O_{10}$ was characterized with the highest dimer signals for experiments with OH

531 exposures under 3.5×10^{10} molecule cm^{-3} s. Nevertheless, $C_{18}H_{26}O_{10}$, together with $C_{18}H_{28}O_{12}$,

532 $C_{18}H_{26}O_{12}$, $C_{18}H_{28}O_{11}$, $C_{18}H_{28}O_{13}$, and $C_{18}H_{28}O_{10}$ contributed more than 50% of total HOM

533 dimer signals at any OH exposure levels (Figure 2b). These six most abundant HOM dimers

534 correspond exactly to the hydroperoxyl, hydroxyl, and carbonyl termination products of

535 $C_{18}H_{27}O_{11}\cdot$ and $C_{18}H_{27}O_{13}\cdot$, respectively. These two RO$_2$ ($C_{18}H_{27}O_{11}\cdot$ and $C_{18}H_{27}O_{13}\cdot$), on the

536 other hand, could be generated by OH attacks to $C_{18}H_{26}O_8$ and $C_{18}H_{26}O_{10}$, respectively, which

537 strongly suggests the significant role of secondary OH chemistry in the formation of HOMs in

538 our experiments. In addition, $C_{18}H_{28}O_x$ can also be formed through accretion of a $C_9H_{13}O_m\cdot$

539 radical and a $C_9H_{15}O_m\cdot$ radical, as suggested by previous studies (Molteni et al., 2018; Wang et

540 al., 2020; Tsiligiannis et al., 2019). However, since a $C_9H_{15}O_m\cdot$ radical, as suggested by its

541 hydrogen atom number, can only be formed via an OH addition to the stabilized $C_9H_{14}O_m$

542 products through multi-generation OH reactions, our conclusion that $C_{18}H_{28}O_x$ are multi-

543 generation OH oxidation products still holds. Figure 4 shows the normalized signals of these

544 abundant HOM dimers at different OH exposures.

545 (a)
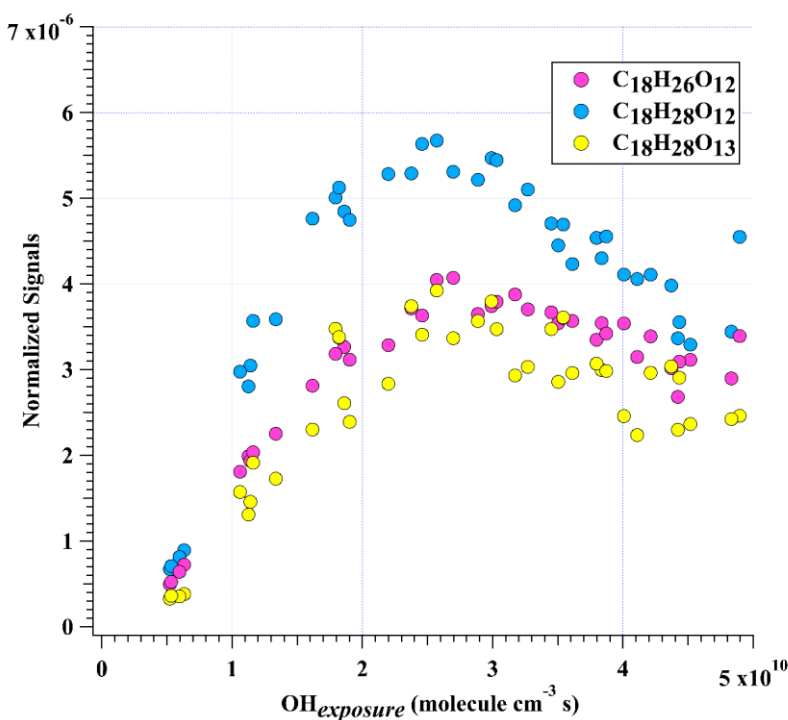
546

547 (b)
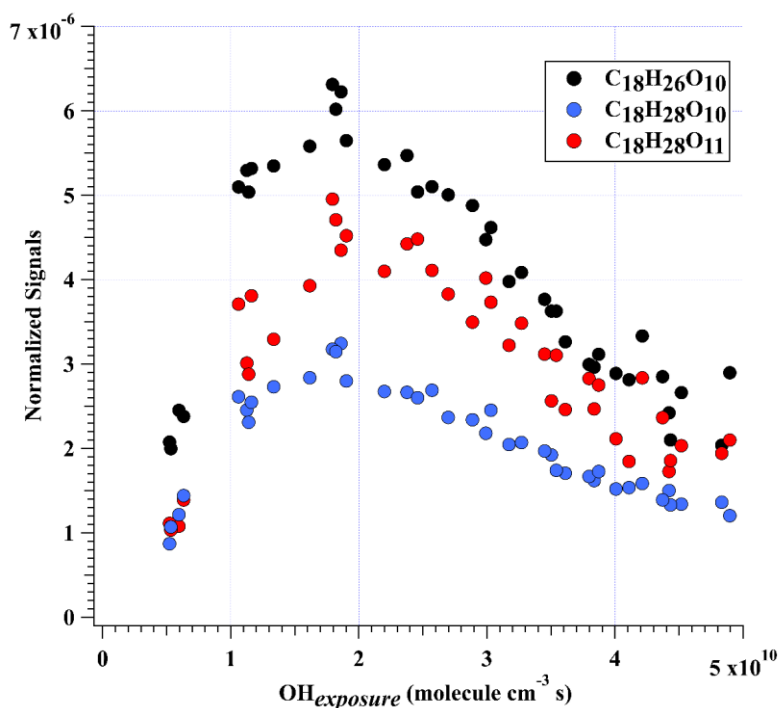
548

549 **Figure 4.** Normalized signals of (a) $C_{18}H_{26}O_{12}$, $C_{18}H_{28}O_{12}$, and $C_{18}H_{28}O_{13}$, and (b) $C_{18}H_{26}O_{10}$,

550 $C_{18}H_{28}O_{10}$, and $C_{18}H_{28}O_{11}$ measured at the exit of OFR in experiments without NO_x as a function

551 of OH exposure.

552

553   This decrease of dimer at relatively high OH exposures are likely due to the accelerated

554 accretion reactions in the OFR, resulted by the high RO_2 concentrations. The HOM dimers are

555 formed earlier compared to under ambient conditions and then can go through the further

556 oxidation reactions. Note that this does not mean the maximum concentrations of HOM dimers

557 will also accurately occur at the same OH exposures in the atmosphere, because the detailed

558 appearance time of the maximum concentrations of HOM dimers is dependent on their

559 formation rate and loss rate. In our experiments, the formation rate and loss rate were not

560 accelerated equally. On the other hand, the loss pathways of HOM dimers were not exactly the

561 same as the ambient due to the lack of aerosols in the OFR. With the decrease of particulate

562 pollution and thus condensation sinks in the polluted areas, the physical loss of HOMs might

563 be lower and the chemical process can be more important. This series of experiments are not

564 meant to specifically find out the detailed OH exposures when the maximum concentrations of

565 HOM dimers will occur, but try to indicate how HOM dimers evolve with the increase of OH

566 exposures. This work can be regarded as an indicator for the potential chemical fates of HOM

567 dimers in the atmosphere. It should be noted that the gas-phase chemistry in the PAM OFR

568 cannot be exactly the same as that in the ambient. Reactions of OH with OVOCs often lead to

569 HO_2 formation, resulting in a HO_2:RO_2 ratio larger than 1 in the real atmosphere (Bianchi et al.,

570 2019). A recent campaign conducted at a rural site in the Yangtze River Delta estimated that

571 the local ratio of $HO_2:RO_2$, the latter of which was presumably derived from longer chain

572 alkanes (> C_3), alkenes, and aromatic compounds, was around 1.66 (Ma et al., 2022). Such a

573 high $HO_2:RO_2$ ratio condition is typically difficult to be simulated in the laboratory experiments,

574 as the precursors are usually hydrocarbons without any OVOCs (Peng and Jimenez, 2020). This

575 is exactly the case for our experiments, but its influences on our conclusion were tiny, as have

576 been discussed in the Section 3.1.Therefore, the difference in the distribution of products will

577 not change our conclusion.

578   Such an active secondary OH chemistry is consistent with the fast OH reaction rates of

579 HOMs. We take $C_{18}H_{26}O_8$ whose plausible structure is shown in Figure S4 as an example,

580 which is the accretion product of two $C_9H_{13}O_5\cdot$. Its OH reaction rate constant is estimated to be

581 around 2.07×10^{-10} cm^3 molecule^{-1} s^{-1} according to the structure-activity relationship (Jenkin et

582 al., 2018b, a), whose details are provided in Supplementary Text S2. This rate is several times

583 larger than that of 1,3,5-TMB, which enables a very active secondary OH chemistry in the

584 system. MCM recommended an OH reaction rate of 1.28×10^{-10} cm^3 molecule^{-1} s^{-1} for

585 TM135BPOOH ($C_9H_{14}O_5$) and 1.00×10^{-10} cm^3 molecule^{-1} s^{-1} for TM135OBPOH ($C_9H_{12}O_4$)

586 (Jenkin et al., 2003). The OH reaction rate for $C_{18}H_{26}O_8$ should also be fast due to the C=C

587 bonds in its structure, which is activated by the adjacent functionalities. Our calculation result

588 is consistent with this estimation.

589   The distributions of C18 organonitrates also verified the extensive secondary reactions.

590 The most abundant C18 organonitrate, $C_{18}H_{27}NO_{12}$ was a NO termination product of radical

591 $C_{18}H_{27}O_{11}\cdot$, which, as mentioned above, was the radical generated from the OH reaction with

592 $C_{18}H_{26}O_8$. $C_{18}H_{27}NO_{12}$ can also be formed either by accretion between a $C_9H_{15}O_m\cdot$ radical and

593 a $C_9H_{12}NO_m\cdot$ radical or accretion between a $C_9H_{13}O_m\cdot$ radical and a $C_9H_{14}NO_m\cdot$ radical. Both

594 $C_9H_{15}O_m\cdot$ and $C_9H_{14}NO_m\cdot$ radicals are a typical multi-generation RO_2 and thus prove

595 $C_{18}H_{27}NO_{12}$ is a multi-generation OH oxidation product. Other C18 organonitrates are believed

596 to be formed in a similar pathway. Hence, plenty of organonitrates have been formed via the

597 multi-generation OH reactions of first-generation stabilized products.

598

599

600 **4 Atmospheric Implications**

601   This study highlights the influences of OH exposure on the distribution and evolution of

602 1,3,5-TMB-derived HOMs. Secondary OH reactions can influence HOMs' composition by

603 directly reacting with the stabilized first-generation oxidation products, leading to enhanced

604 formation of HOMs. Organonitrates generated in the NO experiments further confirmed this.

Due to the elevated abundance and the reduced volatility of HOMs, growth rates of newly formed nanoparticles in the presence of HOMs should be raised, especially in high-OH environments, which prevails in the summer noon. Substantially high concentrations of OH have been frequently observed in polluted environments during summer, e.g., megacities in China (Tan et al., 2019), and thus more active secondary OH reactions are expected compared to wintertime. As a plausible consequence, seasonal differences of HOMs and new particle formation (NPF) are resulted (Qiao et al., 2021; Yao et al., 2018; Guo et al., 2022). Furthermore, previous studies suggest that high concentrations of NO can suppress the formation of HOMs via the suppression of autoxidation (Pye et al., 2019), but the influences of such a suppression could have been overestimated, since secondary OH reactions can continue to oxidize the stabilized organonitrates. Our conclusions help to explain the existing gap between model prediction and ambient measurement on the HOMs concentrations (Qi et al., 2018), and to build a global HOMs simulation model.

Data availability. Data used in this work are available upon request from the corresponding authors.

Supplement. The supplement related to this article is available online.

Author contributions. LW and Yuwei Wang designed the experiments. Yuwei Wang conducted the laboratory experiments. Yuwei Wang analyzed the data. Yuwei Wang and LW wrote the paper. All co-authors discussed the results and commented on the manuscript.

Competing interests. The authors declare that they have no conflict of interest.

Acknowledgments. This work was financially supported by the National Natural Science Foundation of China (21925601, 22127811). The authors declare no competing interests.

References

Berndt, T., Mentler, B., Scholz, W., Fischer, L., Herrmann, H., Kulmala, M., and Hansel, A.: Accretion Product Formation from Ozonolysis and OH Radical Reaction of α-Pinene: Mechanistic Insight and the Influence of Isoprene and Ethylene, Environ. Sci. Technol., 52, 11069–11077, https://doi.org/10.1021/acs.est.8b02210, 2018a.

Berndt, T., Scholz, W., Mentler, B., Fischer, L., Herrmann, H., Kulmala, M., and Hansel, A.: Accretion Product Formation from Self- and Cross-Reactions of RO2 Radicals in the Atmosphere, Angew. Chemie - Int. Ed., 57, 3820–3824, https://doi.org/10.1002/anie.201710989, 2018b.

Bianchi, F., Kurtén, T., Riva, M., Mohr, C., Rissanen, M. P., Roldin, P., Berndt, T., Crounse, J. D., Wennberg, P. O., Mentel, T. F., Wildt, J., Junninen, H., Jokinen, T., Kulmala, M., Worsnop, D. R., Thornton, J. A., Donahue, N., Kjaergaard, H. G., and Ehn, M.: Highly Oxygenated Organic Molecules (HOM) from Gas-Phase Autoxidation Involving Peroxy Radicals: A Key Contributor to Atmospheric Aerosol, Chem. Rev., 119, 3472–3509, https://doi.org/10.1021/acs.chemrev.8b00395, 2019.

Cheng, X., Chen, Q., Li, Y. J., Zheng, Y., Liao, K., and Huang, G.: Highly Oxygenated Organic Molecules Produced by the Oxidation of Benzene and Toluene in a Wide Range of OH Exposure and NOx Conditions, Atmos. Chem. Phys., 1–23, https://doi.org/10.5194/acp-2021-201, 2021.

Crounse, J. D., Nielsen, L. B., Jørgensen, S., Kjaergaard, H. G., and Wennberg, P. O.: Autoxidation of organic compounds in the atmosphere, J. Phys. Chem. Lett., 4, 3513–3520, https://doi.org/10.1021/jz4019207, 2013.

Ehn, M., Thornton, J. A., Kleist, E., Sipilä, M., Junninen, H., Pullinen, I., Springer, M., Rubach, F., Tillmann, R., Lee, B., Lopez-Hilfiker, F., Andres, S., Acir, I. H., Rissanen, M., Jokinen, T., Schobesberger, S., Kangasluoma, J., Kontkanen, J., Nieminen, T., Kurtén, T., Nielsen, L. B., Jørgensen, S., Kjaergaard, H. G., Canagaratna, M., Maso, M. D., Berndt, T., Petäjä, T., Wahner, A., Kerminen, V. M., Kulmala, M., Worsnop, D. R., Wildt, J., and Mentel, T. F.: A large source of low-volatility secondary organic aerosol, Nature, 506, 476–479, https://doi.org/10.1038/nature13032, 2014.

Eisele, F. L. and Tanner, D. J.: Measurement of the gas phase concentration of H 2 SO 4 and methane sulfonic acid and estimates of H 2 SO 4 production and loss in the atmosphere, J. Geophys. Res. Atmos., 98, 9001–9010, https://doi.org/10.1029/93JD00031, 1993.

Garmash, O., Rissanen, M. P., Pullinen, I., Schmitt, S., Kausiala, O., Tillmann, R., Zhao, D., Percival, C., Bannan, T. J., Priestley, M., Hallquist, Å. M., Kleist, E., Kiendler-Scharr, A., Hallquist, M., Berndt, T., McFiggans, G., Wildt, J., Mentel, T. F., and Ehn, M.: Multi-generation OH oxidation as a source for highly oxygenated organic molecules from aromatics, Atmos. Chem. Phys., 20, 515–537, https://doi.org/10.5194/acp-20-515-2020, 2020.

Guo, Y., Yan, C., Liu, Y., Qiao, X., Zheng, F., Zhang, Y., Zhou, Y., Li, C., Fan, X., Lin, Z., Feng, Z., Zhang, Y., Zheng, P., Tian, L., Nie, W., Wang, Z., Huang, D., Daellenbach, K. R., Yao, L., Dada, L., Bianchi, F., Jiang, J., Liu, Y., Kerminen, V. M., and Kulmala, M.: Seasonal variation in oxygenated organic molecules in urban Beijing and their

contribution to secondary organic aerosol, Atmos. Chem. Phys., 22, 10077–10097, https://doi.org/10.5194/acp-22-10077-2022, 2022.

Heinritzi, M., Simon, M., Steiner, G., Wagner, A. C., Kürten, A., Hansel, A., and Curtius, J.: Characterization of the mass-dependent transmission efficiency of a CIMS, Atmos. Meas. Tech., 9, 1449–1460, https://doi.org/10.5194/amt-9-1449-2016, 2016.

Hyttinen, N., Kupiainen-Määttä, O., Rissanen, M. P., Muuronen, M., Ehn, M., and Kurtén, T.: Modeling the Charging of Highly Oxidized Cyclohexene Ozonolysis Products Using Nitrate-Based Chemical Ionization, J. Phys. Chem. A, 119, 6339–6345, https://doi.org/10.1021/acs.jpca.5b01818, 2015.

Iyer, S., Kumar, A., Savolainen, A., Barua, S., Daub, C., Pichelstorfer, L., Roldin, P., Garmash, O., Seal, P., Kurtén, T., and Rissanen, M.: Molecular rearrangement of bicyclic peroxy radicals is a key route to aerosol from aromatics, Nat. Commun., 14, 4984, https://doi.org/10.1038/s41467-023-40675-2, 2023.

Jacob, D. J.: Introduction to atmospheric chemistry, Princeton, 1999.

Jenkin, M. E., Saunders, S. M., Wagner, V., and Pilling, M. J.: Protocol for the development of the Master Chemical Mechanism, MCM v3 (Part B): tropospheric degradation of aromatic volatile organic compounds, Atmos. Chem. Phys., 3, 181–193, https://doi.org/10.5194/acp-3-181-2003, 2003.

Jenkin, M. E., Valorso, R., Aumont, B., Rickard, A. R., and Wallington, T. J.: Estimation of rate coefficients and branching ratios for gas-phase reactions of OH with aliphatic organic compounds for use in automated mechanism construction, 9297–9328 pp., https://doi.org/10.5194/acp-18-9297-2018, 2018a.

Jenkin, M. E., Valorso, R., Aumont, B., Rickard, A. R., and Wallington, T. J.: Estimation of rate coefficients and branching ratios for gas-phase reactions of OH with aromatic organic compounds for use in automated mechanism construction, Atmos. Chem. Phys., 18, 9329–9349, https://doi.org/10.5194/acp-18-9329-2018, 2018b.

Keller-Rudek, H., Moortgat, G. K., Sander, R., and Sörensen, R.: The MPI-Mainz UV/VIS spectral atlas of gaseous molecules of atmospheric interest, Earth Syst. Sci. Data, 5, 365–373, https://doi.org/10.5194/essd-5-365-2013, 2013.

Krechmer, J., Lopez-Hilfiker, F., Koss, A., Hutterli, M., Stoermer, C., Deming, B., Kimmel, J., Warneke, C., Holzinger, R., Jayne, J., Worsnop, D., Fuhrer, K., Gonin, M., and De Gouw, J.: Evaluation of a New Reagent-Ion Source and Focusing Ion− Molecule Reactor for Use in Proton-Transfer-Reaction Mass Spectrometry, Anal. Chem., 90, 12011–12018, https://doi.org/10.1021/acs.analchem.8b02641, 2018.

Lambe, A., Massoli, P., Zhang, X., Canagaratna, M., Nowak, J., Daube, C., Yan, C., Nie, W., Onasch, T., Jayne, J., Kolb, C., Davidovits, P., Worsnop, D., and Brune, W.: Controlled nitric oxide production via O(1D) + N2O reactions for use in oxidation flow reactor studies, Atmos. Meas. Tech., 10, 2283–2298, https://doi.org/10.5194/amt-10-2283-2017, 2017.

Lambe, A., Krechmer, J., Peng, Z., Casar, J., Carrasquillo, A., Raff, J., Jimenez, J., and Worsnop, D.: HO x and NO x production in oxidation flow reactors via photolysis of, 1–22, 2018.

Lambe, A. T., Ahern, A. T., Williams, L. R., Slowik, J. G., Wong, J. P. S., Abbatt, J. P. D., Brune, W. H., Ng, N. L., Wright, J. P., Croasdale, D. R., Worsnop, D. R., Davidovits, P.,

718   and Onasch, T. B.: Characterization of aerosol photooxidation flow reactors:

719   heterogeneous oxidation, secondary organic aerosol formation and cloud condensation

720   nuclei activity measurements, Atmos. Meas. Tech, 4, 445–461,

721   https://doi.org/10.5194/amt-4-445-2011, 2011.

722 Lambe, A. T., Chhabra, P. S., Onasch, T. B., Brune, W. H., Hunter, J. F., Kroll, J. H.,

723   Cummings, M. J., Brogan, J. F., Parmar, Y., Worsnop, D. R., Kolb, C. E., and

724   Davidovits, P.: Effect of oxidant concentration, exposure time, and seed particles on

725   secondary organic aerosol chemical composition and yield, Atmos. Chem. Phys., 15,

726   3063–3075, https://doi.org/10.5194/acp-15-3063-2015, 2015.

727 Lehtipalo, K., Yan, C., Dada, L., Bianchi, F., Xiao, M., Wagner, R., Stolzenburg, D., Ahonen,

728   L. R., Amorim, A., Baccarini, A., Bauer, P. S., Baumgartner, B., Bergen, A.,

729   Bernhammer, A. K., Breitenlechner, M., Brilke, S., Buchholz, A., Mazon, S. B., Chen,

730   D., Chen, X., Dias, A., Dommen, J., Draper, D. C., Duplissy, J., Ehn, M., Finkenzeller,

731   H., Fischer, L., Frege, C., Fuchs, C., Garmash, O., Gordon, H., Hakala, J., He, X.,

732   Heikkinen, L., Heinritzi, M., Helm, J. C., Hofbauer, V., Hoyle, C. R., Jokinen, T.,

733   Kangasluoma, J., Kerminen, V. M., Kim, C., Kirkby, J., Kontkanen, J., Kürten, A.,

734   Lawler, M. J., Mai, H., Mathot, S., Mauldin, R. L., Molteni, U., Nichman, L., Nie, W.,

735   Nieminen, T., Ojdanic, A., Onnela, A., Passananti, M., Petäjä, T., Piel, F., Pospisilova,

736   V., Quéléver, L. L. J., Rissanen, M. P., Rose, C., Sarnela, N., Schallhart, S.,

737   Schuchmann, S., Sengupta, K., Simon, M., Sipilä, M., Tauber, C., Tomé, A., Tröstl, J.,

738   Väisänen, O., Vogel, A. L., Volkamer, R., Wagner, A. C., Wang, M., Weitz, L.,

739   Wimmer, D., Ye, P., Ylisirniö, A., Zha, Q., Carslaw, K. S., Curtius, J., Donahue, N. M.,

740   Flagan, R. C., Hansel, A., Riipinen, I., Virtanen, A., Winkler, P. M., Baltensperger, U.,

741   Kulmala, M., and Worsnop, D. R.: Multicomponent new particle formation from sulfuric

742   acid, ammonia, and biogenic vapors, Sci. Adv., 4, 1–10,

743   https://doi.org/10.1126/sciadv.aau5363, 2018.

744 Li, R., Palm, B. B., Ortega, A. M., Hlywiak, J., Hu, W., Peng, Z., Day, D. A., Knote, C.,

745   Brune, W. H., De Gouw, J. A., and Jimenez, J. L.: Modeling the radical chemistry in an

746   oxidation flow reactor: Radical formation and recycling, sensitivities, and the OH

747   exposure estimation equation, J. Phys. Chem. A, 119, 4418–4432,

748   https://doi.org/10.1021/jp509534k, 2015.

749 Lu, K. D., Rohrer, F., Holland, F., Fuchs, H., Bohn, B., Brauers, T., Chang, C. C., Häseler, R.,

750   Hu, M., Kita, K., Kondo, Y., Li, X., Lou, S. R., Nehr, S., Shao, M., Zeng, L. M.,

751   Wahner, A., Zhang, Y. H., and Hofzumahaus, A.: Observation and modelling of OH and

752   HO2 concentrations in the Pearl River Delta 2006: A missing OH source in a VOC rich

753   atmosphere, Atmos. Chem. Phys., 12, 1541–1569, https://doi.org/10.5194/acp-12-1541-

754   2012, 2012.

755 Ma, X., Tan, Z., Lu, K., Yang, X., Chen, X., Wang, H., Chen, S., Fang, X., Li, S., Li, X., Liu,

756   J., Liu, Y., Lou, S., Qiu, W., Wang, H., Zeng, L., and Zhang, Y.: OH and HO2 radical

757   chemistry at a suburban site during the EXPLORE-YRD campaign in 2018, Atmos.

758   Chem. Phys., 22, 7005–7028, https://doi.org/10.5194/acp-22-7005-2022, 2022.

759 Mehra, A., Wang, Y., E. Krechmer, J., Lambe, A., Majluf, F., A. Morris, M., Priestley, M., J.

760   Bannan, T., J. Bryant, D., L. Pereira, K., F. Hamilton, J., R. Rickard, A., J. Newland, M.,

761   Stark, H., Croteau, P., T. Jayne, J., R. Worsnop, D., R. Canagaratna, M., Wang, L., and

762   Coe, H.: Evaluation of the chemical composition of gas- And particle-phase products of

763   aromatic oxidation, Atmos. Chem. Phys., 20, 9783–9803, https://doi.org/10.5194/acp-

764   20-9783-2020, 2020.

765   Mentel, T. F., Springer, M., Ehn, M., Kleist, E., Pullinen, I., Kurtén, T., Rissanen, M.,

766   Wahner, A., and Wildt, J.: Formation of highly oxidized multifunctional compounds:

767   Autoxidation of peroxy radicals formed in the ozonolysis of alkenes - Deduced from

768   structure-product relationships, Atmos. Chem. Phys., 15, 6745–6765,

769   https://doi.org/10.5194/acp-15-6745-2015, 2015.

770   Mohr, C., Thornton, J. A., Heitto, A., Lopez-hil, F. D., Lutz, A., Riipinen, I., Hong, J.,

771   Donahue, N. M., Hallquist, M., Petäjä, T., Kulmala, M., and Yli-juuti, T.: Molecular

772   identification of organic vapors driving atmospheric nanoparticle growth, Nat.

773   Commun., 1–7, https://doi.org/10.1038/s41467-019-12473-2, 2019.

774   Molteni, U., Bianchi, F., Klein, F., Haddad, I. El, Frege, C., Rossi, M. J., Dommen, J., and

775   Baltensperger, U.: Formation of highly oxygenated organic molecules from aromatic

776   compounds, Atmos. Chem. Phys, 18, 1909–1921, https://doi.org/10.5194/acp-18-1909-

777   2018, 2018.

778   Ng, N. L., Canagaratna, M. R., Zhang, Q., Jimenez, J. L., Tian, J., Ulbrich, I. M., Kroll, J. H.,

779   Docherty, K. S., Chhabra, P. S., Bahreini, R., Murphy, S. M., Seinfeld, J. H.,

780   Hildebrandt, L., Donahue, N. M., Decarlo, P. F., Lanz, V. A., Prévôt, A. S. H., Dinar, E.,

781   Rudich, Y., and Worsnop, D. R.: Organic aerosol components observed in Northern

782   Hemispheric datasets from Aerosol Mass Spectrometry, Atmos. Chem. Phys., 10, 4625–

783   4641, https://doi.org/10.5194/acp-10-4625-2010, 2010.

784   Orlando, J. J. and Tyndall, G. S.: Laboratory studies of organic peroxy radical chemistry: An

785   overview with emphasis on recent issues of atmospheric significance, Chem. Soc. Rev.,

786   41, 6294–6317, https://doi.org/10.1039/c2cs35166h, 2012.

787   Otkjær, R. V., Jakobsen, H. H., Tram, C. M., and Kjaergaard, H. G.: Calculated Hydrogen

788   Shift Rate Constants in Substituted Alkyl Peroxy Radicals, J. Phys. Chem. A, 122, 8665–

789   8673, https://doi.org/10.1021/acs.jpca.8b06223, 2018.

790   Peng, Z. and Jimenez, J. L.: Radical chemistry in oxidation flow reactors for atmospheric

791   chemistry research, Chem. Soc. Rev., 49, 2570–2616,

792   https://doi.org/10.1039/c9cs00766k, 2020.

793   Peng, Z., Day, D. A., Ortega, A. M., Palm, B. B., Hu, W., Stark, H., Li, R., Tsigaridis, K.,

794   Brune, W. H., and Jimenez, J. L.: Non-OH chemistry in oxidation flow reactors for the

795   study of atmospheric chemistry systematically examined by modeling, Atmos. Chem.

796   Phys., 16, 4283–4305, https://doi.org/10.5194/acp-16-4283-2016, 2016.

797   Pye, H. O. T., D'Ambro, E. L., Lee, B. H., Schobesberger, S., Takeuchi, M., Zhao, Y., Lopez-

798   Hilfiker, F., Liu, J., Shilling, J. E., Xing, J., Mathur, R., Middlebrook, A. M., Liao, J.,

799   Welti, A., Graus, M., Warneke, C., de Gouw, J. A., Holloway, J. S., Ryerson, T. B.,

800   Pollack, I. B., and Thornton, J. A.: Anthropogenic enhancements to production of highly

801   oxygenated molecules from autoxidation, Proc. Natl. Acad. Sci. U. S. A., 116, 6641–

802   6646, https://doi.org/10.1073/pnas.1810774116, 2019.

803   Qi, X., Ding, A., Roldin, P., Xu, Z., Zhou, P., Sarnela, N., Nie, W., Huang, X., Rusanen, A.,

804   Ehn, M., Rissanen, M. P., Petäjä, T., Kulmala, M., and Boy, M.: Modelling studies of

805   HOMs and their contributions to new particle formation and growth: comparison of

806   boreal forest in Finland and a polluted environment in China, Atmos. Chem. Phys, 18,
807   11779–11791, https://doi.org/10.5194/acp-18-11779-2018, 2018.

808 Qiao, X., Yan, C., Li, X., Guo, Y., Yin, R., Deng, C., Li, C., Nie, W., Wang, M., Cai, R.,
809   Huang, D., Wang, Z., Yao, L., Worsnop, D. R., Bianchi, F., Liu, Y., Donahue, N. M.,
810   Kulmala, M., and Jiang, J.: Contribution of Atmospheric Oxygenated Organic
811   Compounds to Particle Growth in an Urban Environment, Environ. Sci. Technol.,
812   https://doi.org/10.1021/acs.est.1c02095, 2021.

813 Qu, H., Wang, Y., Zhang, R., Liu, X., Huey, L. G., Sjostedt, S., Zeng, L., Lu, K., Wu, Y.,
814   Shao, M., Hu, M., Tan, Z., Fuchs, H., Broch, S., Wahner, A., Zhu, T., and Zhang, Y.:
815   Chemical Production of Oxygenated Volatile Organic Compounds Strongly Enhances
816   Boundary-Layer Oxidation Chemistry and Ozone Production, Environ. Sci. Technol., 55,
817   13718–13727, https://doi.org/10.1021/acs.est.1c04489, 2021.

818 Riva, M., Rantala, P., Krechmer, J. E., Peräkylä, O., Zhang, Y., Heikkinen, L., Garmash, O.,
819   Yan, C., Kulmala, M., Worsnop, D., and Ehn, M.: Evaluating the performance of five
820   different chemical ionization techniques for detecting gaseous oxygenated organic
821   species, Atmos. Meas. Tech, 12, 2403–2421, https://doi.org/10.5194/amt-12-2403-2019,
822   2019.

823 Slater, E. J., Whalley, L. K., Woodward-Massey, R., Ye, C., Lee, J. D., Squires, F., Hopkins,
824   J. R., Dunmore, R. E., Shaw, M., Hamilton, J. F., Lewis, A. C., Crilley, L. R., Kramer,
825   L., Bloss, W., Vu, T., Sun, Y., Xu, W., Yue, S., Ren, L., Acton, W. J. F., Hewitt, C. N.,
826   Wang, X., Fu, P., and Heard, D. E.: Elevated levels of OH observed in haze events
827   during wintertime in central Beijing, Atmos. Chem. Phys., 20, 14847–14871,
828   https://doi.org/10.5194/acp-20-14847-2020, 2020.

829 Stolzenburg, D., Fischer, L., Vogel, A. L., Heinritzi, M., Schervish, M., Simon, M., Wagner,
830   A. C., Dada, L., Ahonen, L. R., Amorim, A., Baccarini, A., Bauer, P. S., Baumgartner,
831   B., Bergen, A., Bianchi, F., Breitenlechner, M., Brilke, S., Mazon, S. B., Chen, D., Dias,
832   A., Draper, D. C., Duplissy, J., Haddad, I. El, Finkenzeller, H., Frege, C., Fuchs, C.,
833   Garmash, O., Gordon, H., He, X., Helm, J., Hofbauer, V., Hoyle, C. R., Kim, C., Kirkby,
834   J., Kontkanen, J., Kürten, A., Lampilahti, J., Lawler, M., Lehtipalo, K., Leiminger, M.,
835   Mai, H., Mathot, S., Mentler, B., Molteni, U., Nie, W., Nieminen, T., Nowak, J. B.,
836   Ojdanic, A., Onnela, A., Passananti, M., Petäjä, T., Quéléver, L. L. J., Rissanen, M. P.,
837   Sarnela, N., Schallhart, S., Tauber, C., Tomé, A., Wagner, R., Wang, M., Weitz, L.,
838   Wimmer, D., Xiao, M., Yan, C., Ye, P., Zha, Q., Baltensperger, U., Curtius, J.,
839   Dommen, J., Flagan, R. C., Kulmala, M., Smith, J. N., Worsnop, D. R., Hansel, A.,
840   Donahue, N. M., and Winkler, P. M.: Rapid growth of organic aerosol nanoparticles over
841   a wide tropospheric temperature range, Proc. Natl. Acad. Sci. U. S. A., 115, 9122–9127,
842   https://doi.org/10.1073/pnas.1807604115, 2018.

843 Tan, Z., Lu, K., Jiang, M., Su, R., Wang, H., Lou, S., Fu, Q., Zhai, C., Tan, Q., Yue, D.,
844   Chen, D., Wang, Z., Xie, S., Zeng, L., and Zhang, Y.: Daytime atmospheric oxidation
845   capacity in four Chinese megacities during the photochemically polluted season: A case
846   study based on box model simulation, Atmos. Chem. Phys., 19, 3493–3513,
847   https://doi.org/10.5194/acp-19-3493-2019, 2019.

848 Tröstl, J., Chuang, W. K., Gordon, H., Heinritzi, M., Yan, C., Molteni, U., Ahlm, L., Frege,
849   C., Bianchi, F., Wagner, R., Simon, M., Lehtipalo, K., Williamson, C., Craven, J. S.,

850   Duplissy, J., Adamov, A., Almeida, J., Bernhammer, A. K., Breitenlechner, M., Brilke,
851   S., Dias, A., Ehrhart, S., Flagan, R. C., Franchin, A., Fuchs, C., Guida, R., Gysel, M.,
852   Hansel, A., Hoyle, C. R., Jokinen, T., Junninen, H., Kangasluoma, J., Keskinen, H., Kim,
853   J., Krapf, M., Kürten, A., Laaksonen, A., Lawler, M., Leiminger, M., Mathot, S.,
854   Möhler, O., Nieminen, T., Onnela, A., Petäjä, T., Piel, F. M., Miettinen, P., Rissanen, M.
855   P., Rondo, L., Sarnela, N., Schobesberger, S., Sengupta, K., Sipilä, M., Smith, J. N.,
856   Steiner, G., Tomè, A., Virtanen, A., Wagner, A. C., Weingartner, E., Wimmer, D.,
857   Winkler, P. M., Ye, P., Carslaw, K. S., Curtius, J., Dommen, J., Kirkby, J., Kulmala, M.,
858   Riipinen, I., Worsnop, D. R., Donahue, N. M., and Baltensperger, U.: The role of low-
859   volatility organic compounds in initial particle growth in the atmosphere, Nature, 533,
860   527–531, https://doi.org/10.1038/nature18271, 2016.
861   Tsiligiannis, E., Hammes, J., Salvador, C. M., Mentel, T. F., and Hallquist, M.: Effect of NOx
862   on 1,3,5-trimethylbenzene (TMB) oxidation product distribution and particle formation,
863   Atmos. Chem. Phys., 19, 15073–15086, https://doi.org/10.5194/acp-19-15073-2019,
864   2019.
865   Vereecken, L.: Reaction Mechanisms for the Atmospheric Oxidation of Monocyclic Aromatic
866   Compounds, Adv. Atmos. Chem., 377–527,
867   https://doi.org/10.1142/9789813271838_0006, 2019.
868   Wang, S., Wu, R., Berndt, T., Ehn, M., and Wang, L.: Formation of Highly Oxidized Radicals
869   and Multifunctional Products from the Atmospheric Oxidation of Alkylbenzenes,
870   Environ. Sci. Technol., 51, 8442–8449, https://doi.org/10.1021/acs.est.7b02374, 2017.
871   Wang, W., Yuan, B., Peng, Y., Su, H., Cheng, Y., and Yang, S.: Direct observations indicate
872   photodegradable oxygenated VOCs as larger contributors to radicals and ozone
873   production in the atmosphere, Atmos. Chem. Phys., 1–28, 2022.
874   Wang, Y., Mehra, A., Krechmer, J. E., Yang, G., Hu, X., Lu, Y., Lambe, A., Canagaratna, M.,
875   Chen, J., Worsnop, D., Coe, H., and Wang, L.: Oxygenated products formed from OH-
876   initiated reactions of trimethylbenzene: autoxidation and accretion, Atmos. Chem. Phys.,
877   20, 9563–9579, https://doi.org/10.5194/acp-20-9563-2020, 2020.
878   Xu, L., Møller, K. H., Crounse, J. D., Kjaergaard, H. G., and Wennberg, P. O.: New insights
879   into the radical chemistry and product distribution in the OH-initiated oxidation of
880   benzene, Environ. Sci. Technol., 54, 13467–13477,
881   https://doi.org/10.1021/acs.est.0c04780, 2020.
882   Yao, L., Garmash, O., Bianchi, F., Zheng, J., Yan, C., Kontkanen, J., Junninen, H., Mazon, S.
883   B., Ehn, M., Paasonen, P., Sipilä, M., Wang, M., Wang, X., Xiao, S., Chen, H., Lu, Y.,
884   Zhang, B., Wang, D., Fu, Q., Geng, F., Li, L., Wang, H., Qiao, L., Yang, X., Chen, J.,
885   Kerminen, V.-M., Petäjä, T., Worsnop, D. R., Kulmala, M., and Wang, L.: Atmospheric
886   new particle formation from sulfuric acid and amines in a Chinese megacity, Science
887   (80-.)., 361, 278–281, https://doi.org/10.1126/science.aao4839, 2018.
888   Yuan, B., Chen, W., Shao, M., Wang, M., Lu, S., Wang, B., Liu, Y., Chang, C. C., and Wang,
889   B.: Measurements of ambient hydrocarbons and carbonyls in the Pearl River Delta
890   (PRD), China, Atmos. Res., 116, 93–104,
891   https://doi.org/10.1016/j.atmosres.2012.03.006, 2012.
892   Zaytsev, A., Koss, A. R., Breitenlechner, M., Krechmer, J. E., Nihill, K. J., Lim, C. Y., Rowe,
893   J. C., Cox, J. L., Moss, J., Roscioli, J. R., Canagaratna, M. R., Worsnop, D. R., Kroll, J.

894   H., and Keutsch, F. N.: Mechanistic study of the formation of ring-retaining and ring-
895   opening products from the oxidation of aromatic compounds under urban atmospheric
896   conditions, Atmos. Chem. Phys., 19, 15117–15129, https://doi.org/10.5194/acp-19-
897   15117-2019, 2019.
898   Zhao, Y., Thornton, J. A., and Pye, H. O. T.: Quantitative constraints on autoxidation and
899   dimer formation from direct probing of monoterpene-derived peroxy radical chemistry,
900   Proc. Natl. Acad. Sci., 115, 12142–12147, https://doi.org/10.1073/pnas.1812147115,
901   2018.
902